Structural Insights into Kainate Receptor Desensitization

Changping Zhou[1,2], Guadalupe Segura-Covarrubias[1,2], and Nami Tajima[✓1]

[1] Department of Physiology and Biophysics, Case Western Reserve University School of Medicine, Ohio, 44106, USA.

[2]Equal contribution

[✓]Correspondence to nxt193@case.edu (N.T.)

Highlights

1. We present the cryo-EM structure of GluK2 kainate receptors with engineered cysteine crosslinks at the inter-dimer interface, which restricts subunit lateral rotation and attenuates receptor desensitization.
2. The structure of GluK2 double cysteine mutant in complex with the allosteric potentiator BPAM344 and glutamate represents a non-desensitized state, highlighting the critical conformational changes required for ion channel gating.
3. The glutamate-bound GluK2 mutant adopts multiple conformations, representing both shallow- and deep-desensitized states. Electrophysiological recordings indicate that the mutant recovers from desensitization more rapidly, resembling AMPARs. Our structural and functional data suggest that shallow-desensitized KARs remain conductive, implying that the large lateral LBD rotation during KAR desensitization is essential for complete channel closure, distinguishing KARs from other iGluRs.

Keywords

Kainate-type ionotropic glutamate receptors; structure; desensitization mechanism.

Abstract

Kainate receptors (KARs), along with AMPA and NMDA receptors, belong to the ionotropic glutamate receptor (iGluR) family and play critical roles in mediating excitatory neurotransmission throughout the central nervous system. KARs also regulate neurotransmitter release and modulate neuronal excitability and plasticity. Receptor desensitization plays a critical role in modulating the strength of synaptic transmission and synaptic plasticity. While KARs share overall structural similarity with AMPA receptors, the desensitized state of KARs differs strikingly from that of other iGluRs. Despite extensive studies on KAR structure and function, a fundamental question remains unanswered: why do KARs require large conformational changes upon desensitization, unlike other iGluRs? To address this, we present cryo-electron microscopy structures of GluK2 with double cysteine mutations in non-desensitized, shallow-desensitized and deep-desensitized conformations. In the shallow-desensitized conformation, two cysteine crosslinks stabilize the receptors in a conformation that resembles the desensitized state of AMPA receptors. However, unlike the tightly closed pore observed in the deep-desensitized KAR and desensitized AMPAR conformations, the channel pore in the shallow-desensitized state remains incompletely closed. Patch-clamp recordings and fluctuation analysis suggest that this state remains ion-permeable, indicating that the lateral rotational movement of KAR ligand-binding domains (LBDs) is critical for complete channel closure and stable desensitization. Together with the different degrees of desensitized conformations, our results define the unique mechanism and conformational dynamics of KAR desensitization.

50 **Main**

51 Kainate receptors (KARs) belongs to the ionotropic glutamate receptor (iGluR) superfamily
52 together with α-amino-3-hydroxy-5-methyl-4-isoxazolepropionic acid (AMPA), *N*-methyl-d-
53 aspartate (NMDA) and delta receptors. They are a cation selective ligand-gated ion channel
54 activated by an excitatory neurotransmitter glutamate and mediate fast excitatory synaptic
55 transmission in mammalian brains[1,2]. In addition to their major role in mediating the synaptic
56 transmission at post-synapses, KARs also function pre- and extra-synaptically, and regulate
57 excitatory and inhibitory neurotransmitter release and modulate synaptic excitability[3-7]. Abnormal
58 expression and dysfunction of KARs are associated with various neurological diseases and
59 disorders, including schizophrenia, mood disorders, epilepsy, and Huntington's disease[8-17].
60 Therefore, KARs are considered potential therapeutic drug targets due to their physiological and
61 pathophysiological roles[18-21].

62 Kainate receptors (KARs) assemble as homo- or heterotetramers composed of five
63 subunits: GluK1–5[22-25]. Extensive studies revealed that KARs adopt a Y-shaped architecture with
64 four distinct layers: the amino-terminal domain (ATD), which is critical for receptor assembly; the
65 ligand-binding domain (LBD), which contains ligand-binding sites and regulates channel gating;
66 the transmembrane domain (TMD), which forms the ion channel within the plasma membrane;
67 and a short disordered C-terminal domain (CTD), which interacts with intracellular proteins[1,26].
68 Recently determined structures of intact KARs in various liganded states have elucidated the
69 structure-function correlations underlying the mechanisms of activation/desensitization[25,27-31],
70 allosteric modulation[32], inhibition[33], and channel block[34]. A characteristic structural feature of
71 KARs lies in their unique conformation during desensitization. Structures of intact GluK2, first
72 reported in 2014 by the Mayer/Subramaniam lab, have indicated that KAR LBD dimer assemblies
73 are completely dissociated upon desensitization, with a large horizontal-plane rigid-body rotation
74 of the LBDs in the BD subunits, resulting in an approximately four-fold symmetric structures, while

other iGluRs typically retain two-fold symmetric conformations viewed from the top when they are desensitized[26,28]. In addition, a key functional characteristic of KARs is their significantly slower recovery from desensitization — over 50 fold slower compared to AMPARs[35,36]— which limits KAR mediated rapid and high-frequency transmission in neurons[37]. Due to the rapid onset of desensitization induced by the neurotransmitter glutamate, which closes the ion channel within a few milliseconds, previous KAR structures in complex with glutamate have been stabilized in fully or deep-desensitized states, with the ion channel fully closed[25,27-31,33,38-40]. Despite their unique structural and functional features, why only KARs exhibit such a strikingly different conformation, which is not conserved in other iGluRs, and how these drastic conformational changes control receptor gating remains elusive.

To address this outstanding question, we present the cryo-electron microscopy (cryo-EM) structure of the GluK2 KAR in multiple functional states, including non-desensitized, shallow-desensitized, intermediate (between shallow and deep desensitized), and deep-desensitized conformations, using cysteine cross-linking in the presence of glutamate and the positive allosteric modulator BPAM344. The structural comparison revealed that the large in-plane rotation of LBDs in both BD subunits and the resulting twisted motion of the LBD-TM3 linkers are essential for tight ion channel closure and stabilization of receptors in the deep-desensitized state—a feature not observed in AMPARs and NMDARs. Functionally, the crosslinked GluK2 mutant exhibits a large steady-state current, as analyzed by patch-clamp recording. Furthermore, noise analysis of the mutant's fractional steady-state currents suggests that the steady-state current is mediated by conducting desensitized receptors in the presence of glutamate. These structural and functional results show that robust in-plane rotations of the LBDs are essential for proper ion channel closure. Overall, our study provides new insights into the unique desensitization mechanism of the KAR subfamily.

Results

Trapping GluK2 KARs in a non-desensitizing state

Previous studies have shown that LBD dimer reorientations switch the gating of KARs[27-29]. To gain insight into the detailed conformational transitions from active to desensitized states, we first generated a homology model of the full-length GluK2 receptor, comprising the ATD, LBD, and TMD layers based on the structure of the activated GluA2 AMPA receptor in the presence of glutamate, potentiator, and auxiliary subunit in its higher conductive O2 open state (Protein Data Bank (PDB) code 5WEO)[41-43] using SWISS-MODEL[44-48] (Fig. S1A, B). In the model, the G/E helices of subunit A and the K helix of subunit B come into close proximity (Fig. S1C, D), resembling the recently determined structure of GluK2 bound to glutamate, an allosteric positive modulator BPAM344, and Concanavalin A (ConA) in an open state, using time-resolved cryo-EM (PDB code 9B36)[27]. Specifically, the distances between the Cα atoms of K676 in subunit A and N802 in subunit B are 6.2 Å and 6.7 Å in the homology model and the active GluK2 structure, respectively. By contrast, these distances are much greater in the BAPM344-bound (no agonist supplemented) inactive state (PDB code 8FWS)[32], as well as in the antagonized (PDB code 5KUH)[28], and desensitized (PDB code 9B38, 5KUF)[27,28] states (Fig. S1D). Cysteine crosslinking approaches have been used to analyze the dynamics and the channel function of iGluRs[49-53]. Additionally, a recent report showed that the conformational changes of KARs upon activation resembles those of AMPARs[27]. Based on these reports, we hypothesized that an engineered disulfide bond between residues K676 and N802 would restrict the mobility of the LBD and trap a dimer-of-dimers LBD conformation, potentially altering desensitization kinetics. To test this hypothesis, we introduced a pair of cysteine residues designed to form disulfide bonds between the LBD dimer pairs (Fig. S1 E, F) and assessed the channel activity of the full-length rat GluK2 K676C/N802C mutant using whole-cell patch-clamp recordings. Note that the distance between the Cα atoms of two cysteines required to form a disulfide bond is reported to be less than 7 Å[54].

125 The GluK2 wild type (WT) demonstrated the rapid desensitization, as observed
126 previously[35]. By contrast, the GluK2 K676C/N802C mutant, activated by 1 mM glutamate, showed
127 earlier rapid desensitization and a steady-state current (Fig. 1A). When we assessed the GluK2
128 K676C and GluK2 N802C single cysteine mutants, both exhibited nearly complete desensitization,
129 similar to GluK2 WT, without displaying the steady-state current observed in the GluK2
130 K676C/N802C double cysteine mutant (Fig. S2A). These results confirm that disulfide bond
131 formation between K676C and N802C are responsible for generating the steady-state current.

132 An earlier study showed that BPAM344 significantly decreases the desensitization kinetics
133 of GluK2 WT, in addition to potentiating the glutamate-evoked current by 140-fold and 21-fold,
134 respectively[55]. To assess how BPAM344 modulates the activation and desensitization of the
135 GluK2 K676C/N802C mutant, we next analyzed its effect. Indeed, the percent desensitization of
136 GluK2 K676C/N802C elicited by 1 mM glutamate is dramatically decreased in the presence of
137 0.5 mM BPAM344 and only 25% was desensitized after 20 seconds (Fig. 1 A, B). While the peak
138 current amplitude (I_{peak}) was increased 1.5-fold (1.5 ± 0.3, n=10) similar to the WT in the presence
139 of BPAM344, the steady-state current (I_{ss}) amplitudes were also significantly increased
140 approximately 4.7-fold (4.7 ± 0.6, n=10) (Fig. 1C). Thus, we sought to capture the conformation
141 of receptors in this non-desensitizing state using cryo-EM.

142

143 **GluK2 K676C/N802C adopts multiple conformations**

144 We expressed the intact homotetrameric GluK2 KAR incorporating K676C/N802C double
145 cysteine mutations in HEK293S GnTI$^-$ cells and purified the proteins in the detergent, n-Dodecyl-
146 B-D-Maltoside (DDM). The final protein sample (Fig. S2B, C) was pre-incubated with 1 mM
147 glutamate, with or without 0.5 mM BPAM344, prior to grid freezing. We initially performed 3-
148 dimensional (3D) refinement without imposing symmetry (Table S1). Our initial global
149 reconstruction of the glutamate/BPAM344-supplemented dataset generated six main classes (Fig.

150 S3a). One of the classes has a two-fold rotational symmetrical conformation (Fig. 1D), with the
151 extracellular domains resembling the active-state conformation (PDB code 9B36)[27]. To improve
152 the density, we further performed signal subtraction on the ATD and LBD-TMD layers separately.
153 The local refinements with focused masks yielded 3.7 Å and 3.9 Å reconstruction of the ATD and
154 LBD-TMD, respectively, enabling reliable model building (Fig. S3a, S4 A–C). The reconstruction
155 of the LBD-TMD showed clear density for BPAM344 at the LBD dimer interface consistent with
156 previous reports[27,32,56] (Fig. 1E–G). All four LBD bi-lobes are closed in the presence of glutamate,
157 compared to its open conformation in an apo GluK2 (PDB code 9CAZ) structure (Fig. 1H, I). Clear
158 densities corresponding to disulfide bonds between K676C and N802C were observed (Fig. 1J).
159 While the extracellular domain adopts an active-like conformation, the ion channel pore remains
160 closed. Therefore, we refer to this class as a non-desensitized conformation.

161 In contrast, the remaining five classes showed no BPAM344 molecules at the LBD D1-D1
162 interface, leading to D1-D1 rupture. In all of these five classes, the LBD bi-lobes of all four subunits
163 are tightly closed in the presence of glutamate, with closure degrees ranging from 23° to 27°,
164 indicating glutamate binding to the receptors. The overall structures of these five conformations
165 are stabilized in two- or four-fold symmetrical, or asymmetrical arrangements. In order to analyze
166 conformations in the absence of allosteric potentiators, we also collected cryo-EM data of GluK2
167 K676C/N802C supplemented with glutamate. These data revealed four main three-dimensional
168 (3D) classes (Fig. S3b), each are superimposable with the glutamate-bound, BPAM344-unbound
169 classes from the BPAM344-supplemented sample (Fig. S3a). Thus, we combined these two data
170 sets and further performed processing and refinement to improve the density quality. We defined
171 these classes as shallow-desensitized, intermediate, and deep-desensitized states, based on the
172 observations described below. Ultimately, the final resolutions of desensitized classes range from
173 3.7 Å to 4.0 Å (Fig. S4).

174

175 **GluK2 K676C/N802C mutant structure bound to glutamate and BPAM344 represents a non-**
176 **desensitized conformation**

177 While all six 3D reconstructions showed three domains—ATD, LBD, and TMD—as
178 previously reported[25,28,30,31,33], each class showed distinct conformations (Fig. S3). In the non-
179 desensitized structure, two molecules of BPAM344 per LBD dimer bind and stabilize the LBD D1-
180 D1 interfaces, with each BPAM344 forming hydrogen bonds with the side chain of P532, as
181 recently reported[27,32,56] (Fig. 1G). In addition to BPAM344, two disulfide bonds trapped the LBDs
182 in a dimer-of-dimers conformation in the presence of the agonist, as designed. Previously, the
183 structure of active/open GluK2 was determined in the presence of two positive allosteric
184 modulators, concanavalin A (ConA), BPAM344, as well as the agonist glutamate (PDB code
185 9B36)[27]. In the structure, the ~50 kDa ConA dimer, along with BPAM344 and glutamate, binds at
186 the ATD-LBD interface, elevating the ATD by 16 Å and rotating the LBD relative to the ATD layer
187 by 28° (Fig. S5). The same tendency was observed in the presence of NETO auxiliary proteins,
188 which also bind to the ATD and LBD layers and modulate KAR kinetics[30]. Interestingly, a
189 comparison between structures without an orthosteric ligand (PDB codes 8FWQ, 9CAZ)[32] and
190 our non-desensitized structure revealed that the distance between the center of mass (COM) of
191 the ATD and LBD also increased by 7.5 Å in the absence of ConA and NETO auxiliary proteins.
192 By contrast, in the desensitized state, this distance between the ATD and LBD decreased by 2–
193 4 Å compared to the apo state. While, the ATDs in all structures are superimposable and do not
194 undergo any conformational changes (Fig. S5B), the ATD in the non-desensitized class also
195 displayed a rigid-body rotation of 45° counterclockwise (Fig. S5C), following the same movement
196 tendency observed in the open state of KARs[27] and AMPARs[57]

197 Focusing on the LBD layer, the LBDs are stabilized in a dimer-of-dimers arrangement that
198 resembles the open conformation (Fig. 2A), with the D1–D1 association stabilized by BPAM344
199 and the D2–D2 separation maintained in the LBD dimer in the presence of glutamate (Fig. 2B).

200 Analysis of the center-of-mass (COM) distances between D1-D1 and D2-D2 in the two structures
201 further indicates their similar conformational arrangement. Specifically, the distance between the
202 Cα atoms of S670, located at the bottom of the D2 lobes in the AD and BC subunit pairs, is equally
203 separated as seen in the open-state conformation. Key features of the open-state conformation
204 of iGluRs include increased tension in LBD-TM3 linkers and the expansion of the ion channel
205 pore held by the linkers, particularly at the gate region[1,58]. Thus, we next compared the LBD-TM3
206 linker arrangement, TM3 helix orientation, and channel openings in the BPAM344-bound (without
207 an orthosteric ligand), non-desensitized, and open GluK2 conformations. The densities of all TM3
208 helices are well resolved (Fig. S6). In the non-desensitized conformation, the TM3 helices are
209 unwound at A656 in the BD subunits and at E662 in AC subunits (position (3) and (2'),
210 respectively), and therefore, T660 (BD subunits) and M664 (AC subunits) are pulled away from
211 the ion channel central axis, while the BPAM344-bound GluK2 (PDB code 8FWS)[32] displays an
212 additional half-turn of the helix at the pore entrance, and the TM3 helices unwind at T660 in the
213 AC subunits and at M664 in the BD subunits (position (2) and (1), respectively) (Fig. 2C).
214 Consequently, the top of the gating region, which contains the conserved SYTANLAAF motif[59,60],
215 is more dilated in the non-desensitized conformation. By contrast, the TM3 helices in the open
216 GluK2 conformation (PDB code 9B36)[27] display kinking at a deeper position, specifically at L655
217 (position (4)) in all four subunits (Fig. 2D). Additionally, the open conformation exhibits the
218 rotational movements of TM3, which put away T652 from the central axis of the pore, thus opening
219 the channel. However, these rotational movements are not observed in the non-desensitized
220 conformation. Overall, the ion channel in the non-desensitized conformation remains closed (Fig.
221 2E, F).

222

223 **Disulfide bonds between K676C-N802C stabilized GluK2 KARs in a desensitized AMPA**
224 **receptor like conformation**

225 The glutamate-bound, potentiator-unbound GluK2 K676C/N802C generated five classes
226 (Fig. 3A). The LBD layer conformations in these classes appear desensitized; however, they
227 represent different levels of desensitization (Fig. 3B). In one of these desensitized classes, the
228 absence of BPAM344 results in D1–D1 dissociation, a hallmark structural feature of iGluR
229 desensitization, while two disulfide bonds between K676C and N802C (Fig. 3C) stabilize LBD
230 dimers forming a dimer-of-dimers conformation. We refer to this as the 'shallow-desensitized'
231 conformation to distinguish it from the typical deep-desensitized conformations previously
232 observed[28]. Another class, termed the intermediate state, contains an LBD dimer on one side and
233 a disrupted dimer on the other. In this class, one LBD dimer pair maintains its dimer formation
234 with D1–D1 dissociation, resembling the shallow-desensitized state, while the disrupted dimer
235 adopts a conformation characteristic of deep-desensitized classes. Therefore, we propose that
236 this structure represents an intermediate state between the shallow- and deep-desensitized
237 conformations in the presence of glutamate. In contrast, the other three structures lacked inter-
238 subunit disulfide bonds between K676C and N802C, resulting in the LBD layers stabilizing an
239 approximately four-fold symmetric conformation, though with varying in-plane rotation angles of
240 the LBDs (Fig. 3B). We observed the formation of a 'desensitization ring' (Fig. 3D, E) in all three
241 deep-desensitized conformations, consistent with previous reports[28,29,61]. This ring formation plays
242 a key role in regulating desensitization and recovery from desensitization[28,29]. Accordingly, we
243 classified these classes as 'deep-desensitized' states."

244 Comparison of the non-desensitized and shallow-desensitized conformations reveals
245 multiple structural rearrangements in the context of the full-length receptor structure. The distance
246 between the ATD and LBD decreases in the shallow-desensitized state, measuring 2–3 Å shorter
247 than in the apo and BPAM-bound GluK2 structures, making it more similar to the apo state than
248 to the open-state conformations (Fig. S5A). Focusing on the LBD layer, the LBDs in the AC
249 subunits are rotated by 5° parallel to the membrane when viewed from the top, compared to the

250 non-desensitized conformation (Fig. 4A). Viewed from the side, the entire LBDs appear rolled
251 down (Fig. 4B), which is associated with the rearrangement of the dimer-of-dimers formation and
252 the rupture of the D1-D1 interface. These conformational changes are also observed during
253 AMPAR desensitization[43,62-65]. Therefore, we next compared the shallow-desensitized
254 conformation of GluK2 K676C/N802C with the desensitized conformation of GluA2 AMPAR (PDB
255 code 7RYZ)[63]. Viewed from the top, the distance between the Cα atoms of S700 (S662 in GluA2
256 AMPAR) in both structures are reduced compared to their respective open states, although the
257 arrangements in these two structures differ due to the restricted mobility of GluK2 caused by
258 cysteine crosslinks (Fig. 4C). The D1 lobes of GluK2 roll down approximately 25°, in contrast to
259 the 33° rolling-down motion observed in the D1 lobes of GluA2 (Fig. 4D). The D2 distances in the
260 shallow-desensitized GluK2 and desensitized GluA2 are comparable, measuring 20 Å and 24 Å,
261 respectively. Overall, the shallow-desensitized conformation of the GluK2 mutant appears to
262 resemble the desensitized conformation of AMPA receptors. However, this conformation in KAR
263 is energetically unstable and has not been observed in the absence of crosslinks. Comparison of
264 the TM3 in the non-desensitized and shallow-desensitized conformations revealed that the pore
265 in the shallow-desensitized state is occluded at T660, and M663 in the BD and AC subunits,
266 respectively (position (2) and (1)) (Fig. 4E), while the ion channel pore in the deep-desensitized
267 conformations is sealed at M664 in all four subunits (Fig. 4F).

268

269 **A large in-plane rotation of the LBD is required for proper ion channel closure during**
270 **desensitization in GluK2 KAR.**

271 We next assessed the ion channel pore in these desensitized conformations. First, a
272 comparison of the ion channel pore formations in the shallow-desensitized GluK2 KAR and the
273 desensitized GluA2 AMPAR reveals that they are similar (Fig. 5A–C). The shallow-desensitized
274 conformation has restriction points around T652, A656, and T660, which correspond to T617,

275 A621, and T625 in the desensitized GluA2 (PDB code 7RYZ)[63]. The ion channel pore in the
276 transition state is also similar to that in the shallow-desensitized state, with a narrow restriction
277 point (<1 Å) around T652 (Fig. 5D). In contrast, all three deep-desensitized conformations exhibit
278 multiple tight constrictions, particularly at the top of the gate region (Fig. 5E). As previously
279 reported[28,29], the 'desensitization ring' at the bottom of the LBD layers is stabilized by numerous
280 polar interactions, supporting the four-fold symmetrical deep-desensitized conformations,
281 whereas the shallow-desensitized and intermediate conformations exhibit disrupted ring
282 formation, resulting in wider gate regions. Moreover, the significant in-plane rotation of the LBDs
283 in the BD subunits during desensitization twists the LBD-TM3 linker, creating an additional
284 constriction at M664 at the top of the channel pore (Fig. 4F), which is not seen in AMPARs. We
285 observe that the formation of the desensitization ring at the bottom of the LBD layer tightly
286 stabilizes the ion channel in the deep-desensitized conformations, whereas the shallow-
287 desensitized state lacks this secure channel pore lock at T660 and M664 (Fig. 5A).

288 Based on these functional and structural observations, we hypothesize that this GluK2
289 KAR mutant undergoes shallow desensitization rather than deep desensitization, which may allow
290 the receptors to remain ion-permeable, possess a higher open probability, and recover quickly
291 from desensitization, similar to AMPARs, enabling more efficient activation of the receptors.

292

293 **K676C-N802C cysteine crosslinks partially blocks receptors from undergoing deep**
294 **desensitization**

295 To test our hypothesis, we first assessed the kinetics of the GluK2 K676C/N802C mutant
296 using whole-cell patch-clamp electrophysiology. Remarkably, we observed steady-state currents
297 of the cross-link mutant even at the highest concentration of glutamate (50 mM), which were not
298 observed in the wild type GluK2 receptors (Fig. 6A). There were no significant differences neither
299 in the current density at peak current between the GluK2 WT and the mutant (GluK2 WT: 830 ±

300 50 pA/pF, n=6; GluK2 K676C/N802C: 700 ± 150 pA/pF, n=9), nor in the EC_{50} for glutamate (GluK2
301 WT: 110 ± 30 μM, n=7; GluK2 K676C/N802C: 150 ± 50 μM, n=5), indicating that the cysteine
302 crosslinks do not significantly alter agonist binding affinity[66] or desensitization, even at 0.01 mM
303 glutamate, a concentration below the EC_{50} (approximately 0.17 mM). This suggests that partial
304 receptor occupancy is sufficient to trigger desensitization, consistent with earlier findings[67,68].
305 While GluK2 WT desensitizes almost completely with a time constant of 8 ± 1 ms (n=14), the
306 GluK2 K676C/N802C receptors in the presence of 0.01–50 mM glutamate exhibited
307 approximately 60% desensitization, except when activated by 0.001 mM glutamate where only
308 the steady-state current was observed with a decreased peak amplitude. Therefore, the degree
309 of desensitization is not glutamate concentration dependent.

310 To assess the desensitization state or degree of the crosslinked mutant, we next analyzed
311 the rates of recovery from desensitization. As previously reported, recovery from desensitization
312 in the GluK2 WT is extremely slow, requiring 1,150 ± 90 ms (n = 9) for full recovery. By contrast,
313 the GluK2 K676C/N802C mutant exhibited a faster recovery from desensitization, characterized
314 by two distinct components: τ_1 (100 ms, 60%) and τ_2 (1,000 ms, 40%, n = 9). The τ mean of the
315 mutant was 440 ± 40 ms, approximately three times faster than that of the GluK2 WT (Fig. 6F–
316 H). This shift brings its kinetics closer to those of AMPARs, which recover in the order of tens to
317 hundreds of milliseconds (e.g. GluA1 and GluA2 wild-type recovery constants are approximately
318 200 ms and 50 ms, respectively)[66,69]. This result highlights the impact of cysteine cross-linking in
319 accelerating desensitization recovery, potentially by stabilizing shallow-desensitized or pre-active
320 states.

321

322 **The KAR stabilized in a shallow-desensitized conformation remains ion permeable**

323 To assess whether the non-desensitized current and faster recovery kinetics result from
324 crosslinking between the K676C and N802C, we performed whole-cell recordings in the presence

325 of 5 mM dithiothreitol (DTT), applied for 7 minutes prior to the second glutamate activation. The
326 peak intensity of both the WT and the mutant, in the presence and absence of DTT, showed no
327 significant changes, confirming our earlier analysis that the crosslinks do not affect activation
328 kinetics (Fig. 7A). By contrast, the application of 5 mM DTT for 7 minutes significantly reduced
329 the steady-state current of GluK2 K676C/N802C by over 90% (steady-state current prior to and
330 after DTT application: 0.4 ± 0.1 nA and DTT: 0.03 ± 0.03 nA, respectively, n=8) (Fig. 7B).
331 Additionally, recovery from desensitization of the DTT treated cells expressing the mutant was
332 1,040 ms ± 50 (n=5), similar to the WT (Fig. 7C, D). This experiment, along with the assessment
333 of the single cysteine mutants (Fig. S2A), confirmed that the non-desensitizing efficacy we
334 observed is specifically due to the disulfide bonds or to the stabilization of the two-fold symmetrical
335 non-desensitized or shallow-desensitized conformations by the disulfide bonds, as we initially
336 designed.

337 Next, we aimed to determine whether crosslinked receptors remain ion-conductive when
338 exhibiting steady-state current. A key feature of KARs is their exceptionally small conductance
339 and low open-channel probability, which makes it technically challenging to directly observe
340 channel activity at the single-channel level, unlike other channels, including AMPARs[70,71].
341 Therefore, we conducted noise analysis to assess its conductivity. We first performed
342 nonstationary fluctuation analysis (NSFA) on the desensitizing phase of macroscopic currents
343 from GluK2 WT and GluK2 K676C/N802C, activated by glutamate pulses (10 mM, 100 ms). The
344 variance of fluctuations around the expected current was analyzed. The weighted mean single-
345 channel conductance of GluK2 WT was calculated as 23 ± 7.8 pS (n = 5), consistent with previous
346 report[70]. While the current-variance relationship of the wild type was well-fitted by a parabolic
347 function, the analysis of GluK2 K676C/N802C revealed an anomalous current-variance
348 relationship, preventing the calculation of its conductance (Fig. 7E). However, the mutant
349 generates a unique large fractional steady-state current. Thus, we next performed stationary

350 fluctuation on the steady-state current of the desensitized receptors in the presence and absence
351 of BPAM344.

352 To assess unitary conductance and the number of active channels, we analyzed the
353 microscopic currents of GluK2 K676C/N802C activated by 10 mM glutamate for 30 seconds under
354 desensitizing conditions (Fig. 7F). When activated by 10 mM glutamate, the mutant exhibited a
355 unitary conductance of 10 pS—less than half of the wild-type conductance calculated by NSFA—
356 and was similar to the lowest conductive level (O1) previously determined for KARs[70]. Variance-
357 current analysis across individual cells showed that BPAM344 shifted receptor behavior toward
358 higher variance and mean current values (Fig. 7G), suggesting an increase in the number of open
359 receptors and their open probability. Interestingly, the conductance of the mutant activated by 10
360 mM glutamate was similar in the presence and absence of BPAM344 (GluK2 K676C/N802C, 10
361 mM glutamate: 10 ± 3 pS, n = 6; GluK2 K676C/N802C, 10 mM glutamate + 0.5 mM BPAM344:
362 10 ± 2 pS, n = 6) (Fig. 7H). Whereas the number of active channels in the presence of BPAM344
363 was approximately four-fold higher than in its absence (GluK2 K676C/N802C, 10 mM glutamate:
364 1040 ± 600, n = 6; GluK2 K676C/N802C, 10 mM glutamate + 0.5 mM BPAM344: 4080 ± 460, n
365 = 6) (Fig. 7I). In summary, these experiments indicate that desensitized GluK2 K676C/N802C
366 KARs remain conductive at the single channel level, although with significantly lower conductance
367 compared to wild-type channels activated by glutamate.

368

369 **Discussion**

370 Receptor desensitization is a fundamental property of ligand-gated ion channels which
371 depends on agonist, receptor subtypes, and auxiliary proteins. Recent advances in iGluR
372 research have revealed significant differences in the kinetics and conformational dynamics of
373 KARs during desensitization compared to other iGluRs[1,25,28,29,31,33]. The desensitized conformation
374 of KARs is characterized by the quasi-four-fold symmetrical LBDs, by contrast to typical

375 desensitized iGluRs, which remain in two-fold symmetrical conformations. In addition, functionally,
376 the majority of KARs enter deep-desensitized states, with recovery from desensitization occurring
377 over 10-100 times slower than in AMPARs. By contrast, most AMPARs undergo a shallow-
378 desensitized state, with only a minor subset exhibiting deep desensitization under certain
379 conditions[72,73]. In this study, we employed a classical cysteine crosslinking approach to answer
380 the fundamental question why KARs require such dramatical conformational changes for proper
381 channel closure and complete desensitization, which are not conserved in other iGluRs.

382 In the previously determined structure of BPAM344- and ConA-bound GluK2 in a highly
383 ion-conductive open state (O4), ConA binds both the ATD and LBD, occupying the space between
384 these two layers[27]. As a result, the organization of the ATD-LBD layers upon activation remains
385 unclear. To address this, we first analyzed the extracellular domain organization in the absence
386 of ConA. The assembly of the extracellular domains of our glutamate- and BPAM344-bound
387 GluK2 K676C/N802C in the non-desensitized state resembles that of GluK2 in its open state.
388 Interestingly, in the absence of ConA, the ATD-LBD distance in the non-desensitized state of
389 GluK2 K676C/N802C is wider, implicating that the ATD layer is raised and undergoes a
390 counterclockwise in-plane rotation upon activation. By contrast, the apo and desensitized
391 receptors adopt more compact extracellular domain conformations. Since ATD-deleted KARs
392 remain functional as ion channels[27,74], further investigation is needed to determine how these
393 conformational changes in the ATD layer contribute to receptor activation. We also observed the
394 TM3, which form the gating region of the ion channel pore, kinks at the position between the
395 kinking observed in the apo and the O4 open structure (Fig. 8). This observation indicates that
396 TM3 kinking at a higher position (A656/E662) in the gating region does not lead to channel
397 opening, and KAR channel opening indeed requires kinking at a lower position (L655) in all four
398 subunits, distinct from AMPARs[27,41,42,75].

399 Conversely, the glutamate-bound GluK2 K676C/N802C structures represent shallow and
400 deep desensitized conformations as well as the intermediate state between these two states. The
401 shallow-desensitized conformation demonstrates that two inter-dimer crosslinks stabilize
402 receptors in a two-fold symmetrical conformation with D1-D1 ruptured LBDs, similar to the
403 desensitized state of AMPARs[41,43,62-64]. While most previously determined AMPAR structures in
404 desensitized states are stabilized in the classical two-fold symmetrical conformation, the partial
405 agonist, fluorowilliardiine-bound GluA2 AMPAR, in a desensitized state exhibited an asymmetrical
406 conformation with the LBD of subunit D undergoing a large conformational rearrangement similar
407 to our GluK2 in the intermediate-state conformation[76]. Additionally, recent studies have shown
408 that extracellular protons influence extracellular domains and alter LBD conformation, causing
409 minor in-plane rotation of LBDs within the submit B and D, although these changes are not as
410 pronounced as those observed in the deep-desensitized KAR conformations[66,77,78]. Nevertheless,
411 adopting the four-fold symmetrical deep-desensitized conformation is not energetically favorable
412 for AMPARs during desensitization[72], whereas KARs are more stable in this four-fold
413 conformation. Previous mutagenesis studies demonstrated that various mutations in the D2 lobe
414 of KARs alter desensitization and recovery from desensitization, but no mutation completely
415 blocked desensitization unlike AMPARs[61]. This suggests that multiple non-conserved residues
416 contribute to the stability of the four-fold desensitized conformation of KARs, while the overall
417 architecture of AMPAR and KAR LBDs are similar. Our electrophysiological experiments
418 demonstrate that the cysteine crosslinks prevent receptors from undergoing complete
419 desensitization, leading to significantly stronger and faster recovery, mimicking the kinetics of
420 AMPARs rather than those of GluK2 WT. Breaking the disulfide bonds in the GluK2
421 K676C/N802C mutant treated with 5 mM DTT resulted in desensitization recovery similar to that
422 of the WT, demonstrating a correlation between LBD conformation and desensitization recovery
423 of GluK2 KAR.

424 Furthermore, we aimed to answer why KARs have to form the four-fold symmetrical
425 arrangement when desensitized. Previous reports have shown that in the “desensitized ring”, a
426 number of polar interactions stabilizes the deep-desensitized conformation of the LBD layer,
427 resulting in stabilizing the TMD layer conformations and stabilize receptor desensitization and
428 desensitization recovery[28,29]. In the shallow-desensitized conformation, lacking desensitization
429 ring formation with the two-fold symmetric LBDs, we observed that the ion-channel is significantly
430 dilated by contrast to channels observed in desensitized AMPARs and fully/deep desensitized
431 KARs, which show much narrower channel pores throughout the gating region with the channel
432 pore tightly sealed on the top of the gating region. Previously, a conducting desensitized state of
433 AMPAR and acetylcholine receptors has been reported[79,80]. In addition, it was microscopically
434 shown that the partially desensitized KARs are conductive, as defined by the number of
435 desensitized subunits per KAR tetramer[81]. The structural observation together with the
436 characteristic steady-state current of the GluK2 K676C/N802C indicates that the receptors in the
437 shallow-desensitized state could form weakly conductive channels. Indeed, our noise analysis
438 demonstrates that the desensitized GluK2 K676C/N802C receptors, exhibiting steady-state
439 current, remains conductive at the single-channel level; however, its conductance is
440 approximately 30% weaker than the GluK2 WT, regardless of the presence of the positive
441 allosteric modulator BPAM344. In addition, the crosslinked receptors exhibit up to ten-fold faster
442 recovery from desensitization, whereas reducing the disulfide bonds with DTT restores currents
443 similar to those of the GluK2 WT.

444 Taken together, this study answers the fundamental question in that the KARs indeed
445 absolutely require large LBD conformational rearrangements and are stabilized in four-fold
446 symmetrical conformation for proper channel closure and full desensitization into a non-
447 conductive state (Fig. 8). This feature makes KARs unique, as it is not observed in other iGluR
448 subfamilies.

449

450 **Materials and Methods**

451 **Plasmid construction**

452 For Cryo-EM studies, the construct used for the structural studies was full-length rat GluK2 KAR
453 (GenBank 54257, Uniprot code P42260) with two mutations of N802C and K656C. The gene was
454 cloned into the pFW vector (gift from Dr. Hiro Furukawa at Cold Spring Harbor Laboratory) and
455 fused to a C-terminal human rhinovirus 3C protease recognition site and a 1D4 affinity tag. The
456 construct was referred to as GluK2 N802C/K656C.

457

458 **Cell culture**

459 For structural studies, HEK293S GnTI$^-$ cells were grown to a density of 3.2 × 10^6 cells / ml
460 in FreeStyle 293 medium at 37°C and 8% CO_2 supplemented with 2 % fetal bovine serum. The
461 rGluK2 N802C/K676C mutant bacmid and baculovirus were generated as previously described.
462 The P1 and P2 viruses were produced in Sf9 cells. Cells were infected with the baculovirus
463 harboring GluK2 EM and incubated at 37°C for 12 hrs. Cells were supplemented with 10mM
464 sodium butyrate and 20 μM DNQX and temperature was shifted to 30˚C at 12hrs post-infection.
465 The cell culture was incubated additional 60 hrs and harvested by low-speed centrifugation at
466 5,000 g for 20min and stored at -80˚C until use.

467 For electrophysiology experiments, human embryonic kidney 293T (HEK293T) cells were
468 cultured in Dulbecco's modified Eagle medium (DMEM, Corning) supplemented with 10% FBS at
469 37°C in a 95% O_2–5% CO_2 atmosphere. Wild-type rat GluK2 and rat GluK2 K676C/N802C DNAs
470 were cloned into the pCAG-IRES-EGFP vector (Addgene plasmid #119739). HEK293T cells were
471 transfected with 1 μg/μl cDNA using the TransIT2020 transfection reagent (Mirus) according to
472 the manufacturer's instructions. Cells expressing GluK2 wild-type were transfected for 24 hours,
473 while those expressing K676C/N802C were transfected for 18 hours. After transfection, cells were

474 dissociated using Accutase (Innovative Cell Technologies, Inc.), resuspended, and plated onto
475 35 mm poly-D-lysine-coated dishes (Neuvitro). Electrophysiological recordings were performed
476 2–4 hours later[82].
477
478 **Electrophysiological recordings**
479 All whole-cell recordings were performed using HEKA EPC10 amplifiers (HEKA Elektronik,
480 Lambrecht, Germany) with thin-wall borosilicate glass pipettes (2–5 MΩ) coated with dental wax
481 to reduce electrical noise. Currents were recorded at a holding potential of −70 mV, with a
482 sampling frequency of 10 kHz, and filtered at 2.6 kHz. The external solution contained (in mM):
483 145 NaCl, 2.5 KCl, 1.8 $CaCl_2$, 1 $MgCl_2$, 5 glucose, and 5 HEPES. The internal pipette solution
484 contained (in mM): 105 NaCl, 20 NaF, 5 Na_4BAPTA, 0.5 $CaCl_2$, 10 Na_2ATP, and 5 HEPES. The
485 pH and osmotic pressure of the external and internal solutions were adjusted to 7.4 and 300–290
486 mOsm/kg, respectively. L-glutamate was applied using theta glass tubing mounted on a
487 piezoelectric stack (MXPZT-300 series, Siskiyou) driven by a HEKA EPC10 amplifier. Typical 10–
488 90% rise times were 250–300 μs, measured from junction potentials at the open tip of the patch
489 pipette after recordings. Data acquisition was performed using PULSE software (HEKA Elektronik,
490 Lambrecht, Germany).
491
492 **Data analysis**
493 The macroscopic rate of desensitization (τ_desensitization) was measured by fitting an
494 exponential function to the decay of current from ~80% of its peak amplitude (I_peak) to baseline
495 in recordings where glutamate was applied for 1 second. For the double mutant N802C/K676C,
496 only the first exponential component, which exhibited desensitization kinetics, was considered,
497 while the steady-state current was omitted. Desensitization kinetics were fitted using a single-
498 exponential, one-term Levenberg-Marquardt fitting approach.

499 To evaluate recovery from desensitization, two protocols were employed: (1) a two-pulse
500 application of 10 mM glutamate for 100 ms per pulse, with interpulse intervals increasing in 100
501 ms steps from 50 ms to 2 s; and (2) a second protocol with interpulse intervals increasing in 2 s
502 steps, ranging from 50 ms to 20 s. In all cases, the first peak was considered the control (100%
503 activation), while the second peak represented recovery at a given time point. Data from both
504 protocols were combined, and a recovery curve was generated, plotting the percentage of
505 recovery against time. The experimental data were fitted to one-term exponential model, from
506 which the recovery time constant (τ) was derived.

507 To analyze the EC_{50} for glutamate in wild-type (WT) and mutant receptors, varying
508 concentrations of L-glutamate were applied to a single cell using a theta glass tubing mounted on
509 a piezoelectric stack (MXPZT-300 series, Siskiyou), driven by a HEKA EPC10 amplifier, for 1
510 second. One input of the theta glass tubing was connected to the control solution, while the other
511 was connected to a six-inlet manifold for different L-glutamate concentrations. A 2-minute wash
512 was used between concentration changes to ensure complete exchange before applying the next
513 solution. The L-glutamate concentrations tested were 50, 10, 1, 0.1, 0.01, and 0.001 mM, with 50
514 mM serving as the normalization reference. The normalized data are presented as mean ± S.E.M.
515 in a dose-response curve, with response on the y-axis and concentration on the x-axis.
516 Experimental data from independent biological measurements (each defined as data from one
517 cell with at least five concentration responses) were fitted to the Hill equation. The resulting EC_{50}
518 values were then averaged and presented as mean ± S.E.M.

519

520 **Non-stationary fluctuation analysis (NSFA)**

521 NSFA was performed on the decay phase of currents evoked by 200 ms applications of
522 10 mM glutamate (60–150 successive applications). Currents were sampled at 50 kHz and filtered
523 at 5 kHz. The variance and mean current were calculated for each set of currents and then binned
524 into 15 bins. The single-channel current and total number of channels (N) were determined by

plotting the binned variance against the binned mean current and fitting the data with a parabolic function:

$$\sigma^2 = i\bar{I} - \frac{\bar{I}^2}{N} + \sigma_B^2$$

Where σ_B^2 represents the background variance, which was calculated from the baseline before glutamate application. The σ_B^2 value was used to correct the variance, while the mean I_B was used to correct the mean current.

Stationary fluctuation analysis (SFA)

HEK293T cells transfected with GluK2 K676C/N802C were activated with 10 mM glutamate for 30 seconds, followed by a 2-minute incubation with 500 μM BPAM344. The cells were then reactivated with 10 mM glutamate + 500 μM BPAM344. Currents were sampled at 10 kHz and filtered at 2 kHz. For each condition (glutamate alone and glutamate + BPAM344), the last 10 seconds of the steady-state current were used to calculate the variance and mean current. Since the stationary current represented approximately 35% of the peak current, we assumed that the open probability (P_0) in the steady-state current was $P_0 < 1$. The unitary current (i) was then estimated using the following equation:

$$i = \frac{\sigma^2}{\bar{I}}$$

The unitary current was then used to estimate the unitary conductance (γ) as follows:

$$\gamma = \frac{i}{Vm - Vr}$$

where V_m is the holding potential (−70 mV) and the reversal potential (V_r) is 0 mV.

The number of channels (N) was estimated using the equation:

$$N = \frac{\bar{I}^2}{\sigma^2}$$

548 Statistical analyses were performed using OriginLab 2025. Statistical significance was calculated
549 using a two-sided two-sample t-test, with significance assumed if $P < 0.05$.

550

551 **Protein expression and purification**

552 Cell pellets were resuspended in ice-cold lysis buffer containing 20 mM Tris-Cl (pH 8.0),
553 150 mM NaCl, 0.2 mM PMSF, 20 μg/mL DNase I, and 20 μM DNQX. Cells were lysed by
554 sonication using a Qsonica sonicator with an amplitude of 40% for 10 minutes total (10 s on, 10
555 s off). The lysate was centrifuged at 7,000 g for 20 min to remove cell debris and unbroken cells,
556 and the supernatant was subjected to ultracentrifugation at 200,000 g for 30 min to pellet the cell
557 membranes. The membrane pellet was homogenized and solubilized by gentle nutation for 2
558 hours at 4 °C in buffer consisting of 20 mM Tris-Cl (pH 8.0), 150 mM NaCl, 1% Dodecyl-β-D-
559 Maltosid (w/v, DDM), and 20 μM DNQX, followed by centrifugation at 200,000 g for 30 min to
560 remove insoluble material. The supernatant was incubated with Rho 1D4 affinity resin overnight
561 at 4 °C. The protein-bound resin was extensively washed with 100 mL of buffer consisting of 20
562 mM Tris-Cl (pH 8.0), 500 mM NaCl, 1 mM DNQX, and 0.02% DDM at room temperature, and
563 then slowly washed with 200 mL of buffer consisting of 20 mM Tris-Cl (pH 8.0), 300 mM NaCl,
564 and 0.02% DDM at room temperature at a rate of approximately 0.3 ml/min. The protein was
565 eluted in 50 mL of buffer with 20 mM Tris-Cl (pH 8.0), 300 mM NaCl, 0.02% DDM, and 0.25 mM
566 1D4 peptide. The eluted protein was concentrated and injected into a Superose 6 10/300 GL size-
567 exclusion column equilibrated with buffer containing 20 mM Tris-Cl (pH 8.0), 150 mM NaCl, and
568 0.02% DDM. The peak fractions corresponding to tetrameric GluK2 were pooled and
569 concentrated to 3.4 mg/mL for grid freezing.

570

571 **Grid preparation and cryo-EM data**

572 The cryo-EM grids were prepared as follows. UltrAuFoil R1.2/1.3 300 mesh gold grids
573 were glow-discharged for 50 seconds before sample application. A final concentration of 1 mM
574 glutamate was added to the sample, and then a droplet of 3 μL of protein sample was rapidly
575 applied onto the grids. For the BPAM344/glutamate sample, proteins were pre-incubated with 500
576 μM BPAM344 for 30 minutes on ice, followed by the addition of 1 mM glutamate to the sample.
577 3.5 μl of the protein sample was applied to the grids, and the grids are frozen within 10 seconds.
578 An FEI Vitrobot Mark IV (Thermo Fisher Scientific) was used to plunge-freeze the grids into liquid
579 ethane after sample application at 4°C and 100% humidity, with a blot time of 3 seconds and a
580 blot force of −5.

581 All cryo-EM data were collected on a Titan Krios 300 kV microscope (Thermo Fisher
582 Scientific) equipped with a GIF-Quantum energy filter (Gatan) with the slit set to 20 eV and a
583 Gatan K3 Summit direct electron detection camera (Gatan) at Case Western Reserve University.
584 Raw movies were collected using EPU in super-resolution mode, with a physical image pixel size
585 of 1.06 Å and a defocus range of −0.8 to −1.6 μm. The total dose of around 50 e^{-}/Å² was used
586 for each movie, distributed across 50 frames for a total exposure time of approximately 3.2
587 seconds.

588

589 **Cryo-EM image processing**

590 For dataset **a** (GluK2 K676C/N802C supplemented with 1 mM glutamate and 500 μM
591 BPAM344), the same motion correction procedure was applied using Patch Motion Correction in
592 CryoSPARC4. CTF calculations were also carried out on the motion-corrected images using
593 Patch CTF Estimation in CryoSPARC4. Micrographs unsuitable for further analysis were manually
594 removed. Initial particle selection from 1000 micrographs was done with Blob Picker, followed by
595 2D classification to generate good templates. Template Picker was used to pick 903,654 particles,
596 which were extracted with a pixel size of 2.12 Å. After several rounds of 2D classification, 612,540
597 particles were selected for initial 3D model generation via ab initio reconstruction. A total of

598 352,269 particles were selected and re-extracted with a pixel size of 1.06 Å following multiple
599 rounds of heterogeneous refinement. NU-refinement for each class resulted in maps with
600 resolutions of 6.16 Å, 5.80 Å, 4.14 Å, 4.00 Å, 4.00 Å, and 3.83 Å, respectively.

601 For dataset **b** (GluK2 K676C/N802C supplemented with 1 mM glutamate), the raw movie
602 stacks were motion-corrected using Patch Motion Correction in CryoSPARC4. The Contrast
603 Transfer Function (CTF) was calculated from the motion-corrected images using the Patch CTF
604 Estimation in CryoSPARC4. Micrographs deemed unsuitable for further analysis were removed
605 through manual inspection. Initial particle selection was performed using Blob Picker from 2,000
606 micrographs, followed by 2D classification to generate good templates. Subsequently, 1,005,623
607 particles were picked using Template Picker and extracted with a pixel size of 2.12 Å. After several
608 rounds of 2D classification, 765,893 particles were selected to generate the initial 3D model
609 through ab initio reconstruction. A total of 277,369 particles were selected and re-extracted with
610 a pixel size of 1.06 Å after multiple rounds of heterogeneous refinement. NU-refinement for each
611 class yielded maps with resolutions of 3.92 Å, 4.35 Å, 3.85 Å, and 3.82 Å, respectively.

612 To improve the structure resolution for classes present in both datasets, particles from each class
613 were combined and subjected to several rounds of heterogeneous refinement to remove junk
614 particles. Separate NU-refinements for each class generated maps with resolutions of 3.67 Å,
615 4.02 Å, 3.81 Å, and 3.74 Å, respectively. For Class 2, focused masks around the ATD and LBD-
616 TMD regions were created separately and used for local refinements of the corresponding regions.
617 As a result, 3.42 Å reconstruction of the ATD region and 3.86 Å reconstruction of the LBD-TMD
618 region were obtained through local refinement with focused masks. For the non-desensitized state,
619 particle subtraction was performed for both ATD-focused and LBD-TMD-focused heterogeneous
620 refinement. After several rounds of heterogeneous refinement, 80,325 particles were used for
621 subsequent NU-refinement, resulting in a 3.70 Å resolution of the ATD 3D reconstruction. A total
622 of 117,714 particles were subjected to NU-refinement for the LBD-TMD region, generating 3.93
623 Å maps. The Gold-standard Fourier Shell Correlation (FSC) 0.143 criteria were used to estimate

624 the map resolution for each class. For the shallow-desensitized state, focused masks around the
625 ATD and LBD-TMD regions were created separately and used for local refinements of the
626 corresponding regions. As a result, 3.42 Å reconstruction of the ATD region and 3.86 Å
627 reconstruction of the LBD-TMD region were obtained through local refinement with focused
628 masks.
629
630 **Model building and refinement**
631 The model building for the non-desensitized class was initiated by individually fitting rigid-
632 body components of the LBD extracted from the BPAM344-, and ConA-bound GluK2 structure
633 (PDB code 9B36), and the TMD and ATD from the BPAM344 bound GluK2 structure (PDB code
634 8FWQ) into the cryo-EM map using Chimera. Subsequent manual adjustments, including fitting
635 the backbone and side chains of the ATD-LBD and LBD-TM3 linkers into the density, as well as
636 deleting unresolved side chains and making subtle local adjustments to minimize clashes, were
637 performed in Coot.
638 For the shallow-desensitized class, the single LBD, entire ATD, and TMD were separately
639 extracted from the BPAM344 bound GluK2 structure (PDB code 8FWQ) and manually docked
640 into the corresponding cryo-EM map using Chimera. Further manual adjustments of the backbone
641 and side chains were completed in Coot.
642 For intermediate and deep-desensitized classes, the single LBD, entire ATD, and TMD
643 were extracted from the deep-desensitized GluK2 structure (PDB: 5KUF) and individually docked
644 into the corresponding cryo-EM maps for each class using Chimera. Additional manual
645 adjustments to the backbone and side chains were completed in Coot.
646 All four initial models were then refined in real space using Phenix against the
647 corresponding cryo-EM maps. The models were validated through comprehensive validation
648 procedures in Phenix. Glutamate ligands and BPAM344 compounds were extracted from the
649 cryo-EM structure (PDB code 9B36) and manually fitted into the corresponding densities in Coot.

650

651 **Key source table**

Reagent type (species) or resource	**Designation**	**Source or reference**	**Identifiers**	**Additional information**
Gene (*Rattus norvegicus*)	GRIK2_RAT	Genscript (synthesized)	P42260	
Cell line (*Homo sapiens*)	HEK293S GnTI-	ATCC	Cat. No. CRL-3022	
Cell line (*Homo sapiens*)	HEK293T	ATCC	Cat. No. CRL-3216	
Cell line (insect)	Sf9	Novagen	Cat. No. 71104	
Chemical compound, drug	L-glutamate	Sigma Aldrich	Cat. No. 49621	
Software, algorithm	Pulse	HEKA	https://scicrunch.org/resolver/SCR_018399	https://www.heka.com/
Software, algorithm	OriginPro 2020	OriginLab	RRID:SCR_014212	https://www.originlab.com/2020
Software, algorithm	SWISS-MODEL	Expasy		https://swissmodel.expasy.org/interactive

Software, algorithm	cryoSPARC 4.	doi:10.1038/nmeth.4169.	RRID:SCR_016501	https://cryosparc.com/
Software, algorithm	CTFFIND 4.1	doi:10.1016/j.jsb.2015.08.008	RRID:SCR_016732	http://grigoriefflab.janelia.org/ctffind4
Software, algorithm	UCSF Chimera	doi:10.1002/jcc.20084	RRID:SCR_004097	http://plato.cgl.ucsf.edu/chimera/
Software, algorithm	UCSF ChimeraX	doi:10.1002/pro.3943	RRID:SCR_015872	https://www.cgl.ucsf.edu/chimerax/
Software, algorithm	HOLE	doi:10.1016/s0263-7855(97)00009-x		http://www.holeprogram.org
Software, algorithm	COOT 0.9x	doi:10.1107/S0907444910007493	RRID:SCR_014222	http://www2.mrc-lmb.cam.ac.uk/personal/pemsley/coot/
Software, algorithm	Phenix 1.20	doi:10.1107/S2059798319011471	RRID:SCR_014224	https://www.phenix-online.org/
Software, algorithm	MolProbity	doi:10.1107/S0907444909042073	RRID:SCR_014226	http://molprobity.biochem.duke.edu
Software, algorithm	deepEMhancer	https://doi.org/10.1038/s42003-021-02399-1		https://github.com/rsanchezgarc/deepEMhancer

652

Acknowledgment

We thank Dr. Matthias Buck (CWRU) for discussion and critical feedback on the manuscript. We thank Drs. Kunpeng Li and Kyle Whiddon at Case Western Reserve University (CWRU) for their cryo-EM technical support, and the High-Performance Computing Resource CWRU Core facility for their computational support. We are grateful to Drs. Corey Smith and Shyue-An Chan at CWRU for their technical assistance with patch-clamp electrophysiology. We thank Ashlee Hoffman (CWRU) for proofreading the manuscript. This work was funded by the National Institute of Health (1R35GM147266-01 to N.T.), Whitehall Foundation (N.T.), and American Heart Association https://doi.org/10.58275/AHA.23POST1019193.pc.gr.174253 (S.G.).

Author contributions

C.Z., S.G., and N.T. conceived the project and designed the experimental procedures. C.Z. designed the constructs, conduced the protein expression and purification, and performed the EM data collection and data analysis. S.G. conducted electrophysiological recordings. C.Z., S.G., and N.T. wrote the manuscript. All authors reviewed the final draft.

Competing interests

The authors declare no competing interests.

Data and materials availability

Cryo-EM density maps and atomic coordinates for GluK2-apo and GluK2-domoate were deposited in the electron microscopy data bank under the accession codes listed below.

Name	Accession code
GluK2 ATD in the non-desensitized state	PDB 9MZQ, EMD-48765

GluK2 LBD-TMD bound to BPAM344 and glutamate in the non-desensitized state	PDB 9MZR, EMD-48766
GluK2 bound to BPAM344 and glutamate in the non-desensitized state, composite map	PDB 9MZS, EMD-48767
GluK2 ATD in the shallow-desensitized state	PDB 9MZN, EMD-48762
GluK2 LBD-TMD in the shallow-desensitized state	PDB 9MZO, EMD-48763
GluK2 in the shallow-desensitized state, consensus map	PDB 9MZM, EMD-48761
GluK2 in the shallow-desensitized state, composite map	PDB 9MZP, EMD-48764
GluK2 in the intermediate state	PDB 9MZL, EMD-48760
GluK2 in the deep-desensitized state 1	PDB 9MZK, EMD-48759
GluK2 in the deep-desensitized state 2	PDB 9MZJ, EMD-48758
GluK2 in the deep-desensitized state 3	PDB 9MZI, EMD-48757

676

677

678 **Figure legends**

679 **Figure 1. Functional and structural characterization of GluK2 K676C/N802C.**

680 **(A)** Representative whole-cell patch-clamp trace showing response of GluK2 WT or GluK2
681 K676C/N802C to a 20-second application of 1 mM glutamate in the absence and presence of
682 BPAM344 (BPAM). Arrows indicate the maximum peak current (I_{peak}) and the steady-state current
683 (I_{ss}). **(B)** Quantification of percent desensitization for currents evoked by 1 mM glutamate. **(C)**
684 Potentiation of the peak current amplitudes (I_{peak}) of GluK2 WT (left), the peak current amplitudes
685 (I_{peak}) of K676C/N802C (middle), and the steady-state current amplitude (I_{ss}) of GluK2
686 K676C/N802C measured in the presence of BPAM344 compared to currents in the absence of
687 BPAM344. **(D)** Cryo-EM map and model of GluK2 K676C/N802C in complex with glutamate and
688 BPAM344 in a non-desensitized/non-active state. **(E)** Chemical structure of BPAM344. **(F)**

689 Structure of the LBD layer viewed parallel to the membrane, with BPAM344 and glutamate shown
690 as space-filling models, colored pink and cyan, respectively. **(G)** Close-up view of the BPAM344
691 binding site at the AD subunit interface, indicating by a black dotted box in panel F. **(H)**
692 Comparison of the apo GluK2 LBD (PDB code 9CAZ) and the glutamate-bound GluK2 LBD in the
693 non-desensitized LBD conformation. The LBD is a bi-lobed structure, consisting of D1 and D2
694 lobes, with glutamate binding in the cleft between them. The D1 lobe is superimposed, and the
695 rotation angles to align the D2 residues were calculated. The glutamate-bound bi-lobe is closed
696 20° than the apo state LBD conformation. **(I)** Cryo-EM density for bound glutamate and the
697 surrounding residues in the agonist binding pocket. **(J)** The cryo-EM densities for disulfide bonds
698 between K676C and N802C in AB and CD subunits. The crosslinks in the LBD layers are indicated
699 by the red dotted box in the panel F.

700

701 **Figure 2. Structural mechanism of GluK2 upon activation and desensitization.**

702 **(A)** Comparison of Cryo-EM reconstructions and models of BPAM344- and glutamate-bound
703 GluK2 K676C/N802C in a non-desensitized conformation, and BPAM344-, glutamate-, and
704 Concanavalin A-bound GluK2 in an open (active) state (PDB code 9B36). The distances between
705 S700 in the AC subunits and E788 in the BD subunits at the LBD dimer-dimer interface are colored
706 red and blue, respectively. **(B)** Structural comparison of LBD dimers in the non-desensitized and
707 open GluK2, viewed perpendicular to the membrane. The locations of the centers of mass (COM)
708 of D1 and D2 are indicated by blue and green spheres, respectively, with the COM distances
709 between D1 and D2 of subunit AD LBDs (shown as circles) displayed below. Arrows indicate LBD
710 bi-lobe closure, with the D2 lobe moving closer to D1. Distances between the Cα atoms of P773
711 (D1-D1 distance) and S670 (D2-D2 distance) in the AD subunits are also indicated. **(C)**
712 Comparison of LBD-TM3 linkers and TM3 formation in BPAM344-bound, agonist-unbound GluK2
713 (PDB code 8FWS)[32] and non-desensitized GluK2, showing the subunit BD pair (left) and the

714 subunit AC pair (right). S670 is shown as spheres in corresponding colors for the non-
715 desensitized state and in gray for BPAM344-bound GluK2. The cross-dimer distances between
716 the Cα atoms of S670 (in the BD and AC subunit pairs) are indicated above. Residues forming
717 the ion channel pore are displayed as sticks. The locations of the TM3 gating hinge at A656
718 (subunit BD) and E662 (subunit AC) in the non-desensitized conformation are highlighted in red.
719 The dotted line indicates the positions of pore-lining residues: (1) M664, (2) T660, (3) A656, and
720 (4) T652. (2') E662, which forms the gating hinge is also indicated in this panel. Helices
721 surrounding T664 and M664 in subunit BD, as well as helices around M664 in subunit AC, are
722 unwound in the non-desensitized conformation. As a result, the ion channel pore above the gating
723 region in the non-desensitized conformation is wider compared to that in the BPAM344-bound
724 GluK2 structure, with black allows indicating the conformational changes. **(D)** Comparison of LBD-
725 TM3 linkers and TM3 formation in non-desensitized GluK2 and BPAM344-, ConA- and glutamate
726 bound open GluK2 (PDB code 9B36)[27], showing the subunit BD pair (left) and subunit AC pair
727 (right). The cross-dimer distances between the Cα atoms of S670 are indicated above. Residues
728 forming the ion channel pore are displayed as sticks. The locations of the gating hinge at L655 in
729 A-D subunits of the open GluK2 (9B36) structure are highlighted in gray, for comparison with the
730 gating hinge in the non-desensitized conformation shown in panel C. The dotted line indicates the
731 positions of pore-lining residues: (1) M664, (2) T660, (3) A656, and (4) T652, as well as (4') L655,
732 which forms the gating hinge. Arrows indicate the rearrangement of TM3 in the non-desensitized
733 conformation from the open to non-desensitized GluK2 structures. **(E)** Pore profile in the non-
734 desensitized conformation and open (9B36) structure. Pore-delineating dots are colored
735 according to pore radius: red for regions with a radius less than 1.1 Å and gray for regions with a
736 radius greater than 1.1 Å, which would allow passage of a dehydrated ion (1.1 Å for calcium). **(F)**
737 The pore radius for the non-desensitized (red) and open (9B36, gray) calculated using HOLE.

738

739 **Figure 3. Structures of GluK2 in desensitized states.**

740 **(A)** Three-dimensional cryo-EM reconstructions of glutamate-bound GluK2 K676C/N802C in
741 desensitized conformations. **(B)** Top views of glutamate-bound GluK2 K676C/N802C, focusing
742 on the LBD layers. The in-plane rotation angles of the LBDs are indicated. Disulfide bonds formed
743 between the two LBD dimers are highlighted in red dotted boxes. **(C)** Close-up view of the disulfide
744 bonds between K676C and N802C at the CD subunit interface (left) and the AC subunit interface
745 (right) in the shallow-desensitized conformation. **(D)** Top view of the LBD layer in the deep-
746 desensitized conformation, highlighting helices E and G, which form the desensitization ring. The
747 view is parallel to the membrane, with coloring consistent with panel A. **(E)** The desensitization
748 ring formed in three deep-desensitized conformations, viewed perpendicular to the membrane.
749 The in-plane rotation of the LBD shown in panel B shifts the LBD-TM3 linker, positioning it above
750 the ion channel pore formed by the TM3 helices.

751

752 **Figure 4. GluK2 stabilized in a shallow-desensitized like conformations is similar to the**
753 **desensitized AMPAR conformation.**

754 **(A, B)** Structural comparison between the non-desensitized and shallow-desensitized
755 conformations, viewed parallel and perpendicular to the membrane. Black arrows indicate the
756 degree of LBD domain rotation. **(C, D)** Structural comparison of LBD layers in GluK2
757 K676C/N802C in the shallow-desensitized state and GluA2 AMPAR in the desensitized state
758 (PDB code 7RYZ)[63], viewed parallel and perpendicular to the membrane. Distances between
759 S700 in the AC subunits and E788 in the BD subunits at the LBD dimer-dimer interface are color
760 red and blue, respectively. The locations of the centers of mass (COM) of D1 and D2 are indicated
761 by blue and green spheres, respectively, with the COM distances between D1 and D2 of subunit
762 AD LBDs (shown as circles) displayed below. Arrows indicate D1 lobe rotations compared to the
763 non-desensitized (KAR) or apo (AMPAR) states. Distances between the Cα atoms of P773 (D1-

764 D1 distance) and S670 (D2-D2 distance) in the AD subunits are also indicated. **(E)** Comparison
765 of LBD-TM3 linkers and TM3 helices in non-desensitized and shallow-desensitized conformations,
766 showing the subunit BD pair (left) and subunit AC pair (right). S670 is shown as spheres in
767 corresponding colors for the shallow-desensitized conformation and in gray for the non-
768 desensitized conformation. The cross-dimer distances between the Cα atoms of S670 are
769 indicated. Residues forming the ion channel pore are displayed as sticks. The locations of the
770 TM3 gating hinge at T660 (subunit BD) and M664 (subunit AC) in the shallow-desensitized
771 conformation are highlighted in red. The dotted line indicates the positions of pore-lining residues:
772 (1) M664, (2) T660, (3) A656, and (4) T652. The shallow-desensitized conformation contains an
773 additional half-turn of helices at T660 compared to the non-desensitized conformation. **(F)**
774 Comparison of LBD-TM3 linkers and TM3 formation in shallow- and deep-desensitized GluK2,
775 showing the subunit BD pair (left) and the subunit AC pair (right). S670 is represented as spheres
776 in corresponding colors for the deep-desensitized state and in gray for the shallow-desensitized
777 GluK2. The cross-dimer distances between the Cα atoms of S670 are indicated. In the deep-
778 desensitized conformation, the ion channel is sealed at M664, completely closing the ion channel
779 pore, in contrast to the shallow-desensitized conformation, which has a kink at T660 in the BD
780 subunits.

781

782 **Figure 5. Ion channel pore of desensitized GluK2 KAR.**

783 **(A)** Permeation pathway dictating pore diameter of GluK2 K676C/N802C in desensitized states.
784 Pore-delineating dots are colored according to pore radius: red for regions with a radius less than
785 1.1 Å and gray for regions with a radius greater than 1.1 Å. **(B)** Permeation pathway determining
786 the pore diameter of the GluA2 AMPAR in a desensitized state (PDB code 7RYZ)[63], using the
787 same color code as (A). (C–E) Pore profile traces comparing GluK2 K676C/N802C KAR:

788 **(C)** Comparison between the shallow-desensitized conformation and the desensitized GluA2
789 AMPAR (PDB: 7RYZ); **(D)** Comparison between the shallow-desensitized and intermediate
790 (asymmetrical) states; and **(E)** Comparison among three deep-desensitized states.

791

792 **Figure 6. Functional characterization of GluK2 K676C/N802C receptor.**

793 **(A)** Representative whole-cell patch-clamp recordings of GluK2 WT (left) and GluK2
794 K676C/N802C (right) in response to varying concentrations of glutamate (0.001–50 mM). The
795 black bar at the top of the recording represents the glutamate application. The cells were held at
796 -70 mV. **(B)** Quantification of current density (pA/pF) at the peak current for GluK2 WT (gray) and
797 K676C/N802C mutant (blue) activated by 10 mM glutamate. No significant differences were
798 observed (NS, $p > 0.05$). **(C)** Glutamate dose-response curves for GluK2 WT (n=12) and
799 K676C/N802C (n=8), normalized to the maximal response at 50 mM glutamate. Glutamate was
800 applied for 1 s, and the peak current was measured at each concentration. All response were
801 recorded at each concentrations using a single cell. **(D)** EC_{50} values for glutamate activation of
802 GluK2 WT (gray) and K676C/N802C (blue). No significant differences were detected (NS, $p >$
803 0.05). **(E)** Ratio of steady-state to peak current ($I_{steady\text{-}state}$ / I_{peak}) at various glutamate
804 concentrations. The values of the steady-state current were taken at the end of the activation. **(F)**
805 Representative current traces of GluK2 WT (black) and GluK2 K676C/N802C (blue) during a two-
806 pulse protocol, showing the interval between glutamate exposures ranging from 50 ms to 20 s,
807 highlighting altered desensitization kinetics in the mutant. **(G)** Recovery from desensitization at
808 increasing inter-sweep intervals, fitted with one-term exponential functions for GluK2 WT
809 (R^2=0.99) and two-term exponential functions for GluK2 K676C/N802C (R^2=0.99). GluK2
810 K676C/N802C exhibits a faster recovery than the WT. **(H)** Time constant (τ) of recovery from
811 desensitization, showing a significant reduction in τ for the K676C/N802C mutant ($p < 0.0001$,
812 two-sided two-sample t-test). The data for the WT was obtained from the fit in panel G, and for

813 K676C/N802C, a mean τ was calculated using τ_{mean} = ((A1 τ1 + A2 τ2) / (A1 + A2)). Biological
814 independent measurements: n=9 for GluK2 WT and n=9 for K676C/N802C.

815 Error bars represent Standard Deviation (SD). Statistical significance is indicated as NS (not
816 significant) or with p-values where appropriate.

817

818 **Figure 7. Cysteine crosslinking modulates the kinetics of GluK2 K676C/N802C**

819 **(A)** Representative whole-cell patch-clamp recordings of GluK2 WT (left) and GluK2
820 K676C/N802C (right) in the presence of 10 mM glutamate before (black) and after treatment with
821 5 mM DTT for 7 minutes (red). **(B)** Quantification of the I_{ss}/I_{peak} ratio in GluK2 K676C/N802C before
822 (blue) and after (red) DTT treatment, showing a significant reduction in steady-state current
823 following treatment ($p < 0.0001$, two-sided two-sample t-test). **(C)** Recovery from desensitization
824 at increasing inter-sweep intervals after treatment with 5 mM DTT. The GluK2 WT recovery curve
825 from Figure 6, panel C is shown in black for comparison. The recovery kinetics of GluK2
826 K676C/N802C post-DTT treatment were fitted with a one-term exponential function ($R^2 = 0.98$),
827 showing a recovery profile similar to WT. **(D)** Time constant (τ) of recovery from desensitization,
828 showing that DTT treatment restores the recovery kinetics of GluK2 K676C/N802C to a level
829 comparable to WT (NS, $p > 0.05$). **(E)** Representative whole-cell responses to 10 mM glutamate
830 (200 ms, -70 mV; black bar) from HEK293T cells expressing GluK2 WT (left, average current in
831 black, 60 individual responses in gray) and GluK2 K676C/N802C (right, average current in blue,
832 100 individual responses in gray). Inset: Current-variance relationship, with WT data fitting a
833 parabolic function (dotted line), whereas the K676C/N802C mutant does not follow this trend. **(F)**
834 Whole-cell recordings of GluK2 K676C/N802C in response to 10 mM glutamate in the absence
835 (blue) and presence (green) of 500 μM BPAM344. Right panel: Representative noise traces at
836 the end of glutamate application (~10 s) under both conditions, indicated by blue and green boxes.
837 Background noise (baseline) was taken from the current recording before glutamate application,

838 as indicated by the gray box. **(G)** Variance-mean current relationship for individual cells in the
839 presence of glutamate alone or with BPAM344, indicating an increase in channel variance-current
840 relationship after modulator application. Data were obtained from currents shown in panel F. **(H)**
841 Unitary conductance determined by variance-mean analysis, showing no significant difference
842 between conditions (NS, $p > 0.05$). (I) Estimated number of open channels, showing a significant
843 increase after BPAM344 application ($p = 0.0025$, two-sided paired t-test). Biologically
844 independent measurements: $n = 6$. Data for glutamate and BPAM344 conditions were obtained
845 from the same cell.

846 Error bars represent standard deviation (SD). Statistical significance is indicated as NS (not
847 significant) or with p-values where appropriate.

848

849 **Figure 8. Schematic representation of conformational rearrangements during activation**
850 **and desensitization.** The proposed model illustrates how conformational changes in the LBD
851 layers during desensitization regulate ion channel permeation. Wild-type GluK2 typically
852 transitions into a deeply desensitized state, adopting a stabilized, classically four-fold symmetrical
853 conformation. By contrast, receptors that stabilize in a two-fold symmetrical, desensitized
854 AMPAR-like conformation, maintained by engineered disulfide bonds, remain conductive, while
855 the conductivity is lower than those of the receptors in the open state. The gating kinks differ
856 among the non-desensitized, open, and shallow-desensitized conformations. The ATD layers
857 also elevate and rotate in the non-desensitized (inactive) and open-state receptors.

858

859 **Figure S1. Design of the double cysteine crosslink mutant of GluK2.**

860 **(A)** Schematic illustration of the KAR subunit topology. Each KAR subunit is composed of four
861 domains: ATD, LBD,TMD, and CTD. The LBD contains two segments termed D1 (upper lobe)
862 and D2 (lower lobe). Agonists bind to the interface between the D1 and D2 lobes of the LBD. **(B)**

863 Homology model of the active GluK2 KAR, generated based on the active GluA2 AMPAR (PDB
864 code 5WEO) as a template. **(C)** The inter-protomer interface between subunit A and subunit B in
865 the homology model. **(D)** The distance between residues K676 and N802 in the BPAM344-,
866 concanavalin A-, and glutamate-bound active/open GluK2 (PDB code 9B36)[27], BPAM344-bound
867 (without orthosteric ligands) inactive GluK2 (PDB code 8FWS)[32], and glutamate-bound deep
868 desensitized GluK2 (PDB code 9B38)[27] structures. **(E, F)** Two designed disulfide crosslinks at the
869 inter-protomer interface, shown in the homology model and the schematic figure.

870

871 **Figure S2. Channel properties of the single cysteine mutant and protein preparation.**

872 **(A)** Representative electrophysiological traces from HEK293T cells expressing GluK2 WT, GluK2
873 K676C, and GluK2 N802C, activated by 10 mM glutamate. **(B)** Size exclusion chromatography
874 profile of the GluK2 N802C/K676C mutant eluted from the Superose 6 column chromatography.
875 The fractions used for the cryo-EM studies are indicated by the black dotted line. **(C)** SDS-PAGE
876 analysis of the purified GluK2 N802C/K676C mutant, with the black line indicating the full-length
877 GluK2 protein band.

878

879 **Figure S3. Cryo-EM data processing workflow for structures of the GluK2 K676C/N802C**
880 **mutant in the presence of glutamate and BPAM344 (a), and glutamate alone (b)**

881

882 **Figure S4. Cryo-EM analysis of GluK2 K676C/N802C.**

883 **(A, D)** Local resolution maps, **(B, E)** Fourier shell correlation (FSC) curves. The threshold was set
884 at 0.143 for unmasked and masked curves, and a 0.5 threshold was used for the map-to-model
885 curve. **(C, F)** Angular distribution of particles calculated using the 3D refinement reconstruction
886 algorithm in cryoSPARC.

887

888 **Figure S5. Comparison of ATD-LBD layers.**

889 **(A)** GluK2 structures, aligned parallel to the membrane. The distances between the center-of-
890 mass (COM, black circles) of the ATD and LBD layers are indicated. **(B)** Superimposition of the
891 ATD layer in the non-desensitized, intermediate, and desensitized GluK2 structures. The color
892 codes match those in panel A. **(C)** ATD-LBD rotation. The LBD layers in the BPAM344- and
893 glutamate-bound non-desensitized, and the BPAM344-, ConA-, and glutamate-bound open
894 GluK2 conformations, are rotated counterclockwise when the ATD layers are superimposed.

895

896 **Figure S6. Models and cryo-EM densities of the transmembrane domain.**

897 TM3 helices in non-desensitized, shallow-desensitized, intermediate, and deep-desensitized
898 structures, with the protein structural model shown as ribbons and sticks. Cryo-EM densities are
899 displayed in transparent gray.

900

901

902 **References**

903

904 1 Hansen, K. B. *et al.* Structure, Function, and Pharmacology of Glutamate Receptor Ion
905 Channels. *Pharmacol Rev* **73**, 298-487 (2021).
906 https://doi.org:10.1124/pharmrev.120.000131

907 2 Lerma, J. Roles and rules of kainate receptors in synaptic transmission. *Nat Rev Neurosci*
908 **4**, 481-495 (2003). https://doi.org:10.1038/nrn1118

909 3 Chittajallu, R. *et al.* Regulation of glutamate release by presynaptic kainate receptors in
910 the hippocampus. *Nature* **379**, 78-81 (1996). https://doi.org:10.1038/379078a0

911 4 Rodríguez-Moreno, A., Herreras, O. & Lerma, J. Kainate receptors presynaptically
912 downregulate GABAergic inhibition in the rat hippocampus. *Neuron* **19**, 893-901 (1997).
913 https://doi.org:10.1016/s0896-6273(00)80970-8

914 5 Cossart, R. *et al.* Presynaptic kainate receptors that enhance the release of GABA on CA1
915 hippocampal interneurons. *Neuron* **29**, 497-508 (2001). https://doi.org:10.1016/s0896-
916 6273(01)00221-5

917 6 Polenghi, A. *et al.* Kainate Receptor Activation Shapes Short-Term Synaptic Plasticity by
918 Controlling Receptor Lateral Mobility at Glutamatergic Synapses. *Cell Rep* **31**, 107735
919 (2020). https://doi.org:10.1016/j.celrep.2020.107735

920 7 Ramos, C. *et al.* Activation of Extrasynaptic Kainate Receptors Drives Hilar Mossy Cell
921 Activity. *J Neurosci* **42**, 2872-2884 (2022). https://doi.org:10.1523/jneurosci.0922-21.2022

922 8 Lerma, J. & Marques, J. M. Kainate receptors in health and disease. *Neuron* **80**, 292-311
923 (2013). https://doi.org:10.1016/j.neuron.2013.09.045

924 9 Aller, M. I., Pecoraro, V., Paternain, A. V., Canals, S. & Lerma, J. Increased Dosage of
925 High-Affinity Kainate Receptor Gene grik4 Alters Synaptic Transmission and Reproduces
926 Autism Spectrum Disorders Features. *J Neurosci* **35**, 13619-13628 (2015).
927 https://doi.org:10.1523/jneurosci.2217-15.2015

928 10 Begni, S. *et al.* Association between the ionotropic glutamate receptor kainate 3 (GRIK3)
929 ser310ala polymorphism and schizophrenia. *Mol Psychiatry* **7**, 416-418 (2002).
930 https://doi.org:10.1038/sj.mp.4000987

931 11 Shaltiel, G. *et al.* Evidence for the involvement of the kainate receptor subunit GluR6
932 (GRIK2) in mediating behavioral displays related to behavioral symptoms of mania. *Mol*
933 *Psychiatry* **13**, 858-872 (2008). https://doi.org:10.1038/mp.2008.20

934 12 Shibata, H. *et al.* Association study of polymorphisms in the GluR7, KA1 and KA2 kainate
935 receptor genes (GRIK3, GRIK4, GRIK5) with schizophrenia. *Psychiatry Res* **141**, 39-51
936 (2006). https://doi.org:10.1016/j.psychres.2005.07.015

937 13 Diguet, E. *et al.* Experimental basis for the putative role of GluR6/kainate glutamate
938 receptor subunit in Huntington's disease natural history. *Neurobiol Dis* **15**, 667-675 (2004).
939 https://doi.org:10.1016/j.nbd.2003.12.010

940 14 Schiffer, H. H. & Heinemann, S. F. Association of the human kainate receptor GluR7 gene
941 (GRIK3) with recurrent major depressive disorder. *Am J Med Genet B Neuropsychiatr*
942 *Genet* **144b**, 20-26 (2007). https://doi.org:10.1002/ajmg.b.30374

943 15 Pickard, B. S. *et al.* A common variant in the 3'UTR of the GRIK4 glutamate receptor gene
944 affects transcript abundance and protects against bipolar disorder. *Proc Natl Acad Sci U*
945 *S A* **105**, 14940-14945 (2008). https://doi.org:10.1073/pnas.0800643105

946 16 Catches, J. S., Xu, J. & Contractor, A. Genetic ablation of the GluK4 kainate receptor
947 subunit causes anxiolytic and antidepressant-like behavior in mice. *Behav Brain Res* **228**,
948 406-414 (2012). https://doi.org:10.1016/j.bbr.2011.12.026

949 17 Lowry, E. R., Kruyer, A., Norris, E. H., Cederroth, C. R. & Strickland, S. The GluK4 kainate
950 receptor subunit regulates memory, mood, and excitotoxic neurodegeneration.
951 *Neuroscience* **235**, 215-225 (2013). https://doi.org:10.1016/j.neuroscience.2013.01.029

952 18 Matute, C. Therapeutic potential of kainate receptors. *CNS Neurosci Ther* **17**, 661-669
953 (2011). https://doi.org:10.1111/j.1755-5949.2010.00204.x

954 19 Jane, D. E., Lodge, D. & Collingridge, G. L. Kainate receptors: pharmacology, function
955 and therapeutic potential. *Neuropharmacology* **56**, 90-113 (2009).
956 https://doi.org:10.1016/j.neuropharm.2008.08.023

957 20 Negrete-Díaz, J. V., Falcón-Moya, R. & Rodríguez-Moreno, A. Kainate receptors: from
958 synaptic activity to disease. *Febs j* **289**, 5074-5088 (2022).
959 https://doi.org:10.1111/febs.16081

960 21 Swanson, G. T. Targeting AMPA and kainate receptors in neurological disease: therapies
961 on the horizon? *Neuropsychopharmacology* **34**, 249-250 (2009).
962 https://doi.org:10.1038/npp.2008.158

963 22 Cui, C. & Mayer, M. L. Heteromeric kainate receptors formed by the coassembly of GluR5,
964 GluR6, and GluR7. *J Neurosci* **19**, 8281-8291 (1999).
965 https://doi.org:10.1523/jneurosci.19-19-08281.1999

966 23 Mulle, C. *et al.* Subunit composition of kainate receptors in hippocampal interneurons.
967 *Neuron* **28**, 475-484 (2000). https://doi.org:10.1016/s0896-6273(00)00126-4

968 24 Reiner, A., Arant, R. J. & Isacoff, E. Y. Assembly stoichiometry of the GluK2/GluK5 kainate
969 receptor complex. *Cell Rep* **1**, 234-240 (2012).
970 https://doi.org:10.1016/j.celrep.2012.01.003

971 25 Selvakumar, P. *et al.* Structural and compositional diversity in the kainate receptor family.
972 *Cell Rep* **37**, 109891 (2021). https://doi.org:10.1016/j.celrep.2021.109891

973 26 Mayer, M. L. Structural biology of kainate receptors. *Neuropharmacology* **190**, 108511
974 (2021). https://doi.org:10.1016/j.neuropharm.2021.108511

975 27 Gangwar, S. P. *et al.* Kainate receptor channel opening and gating mechanism. *Nature*
976 (2024). https://doi.org:10.1038/s41586-024-07475-0

977 28 Meyerson, J. R. *et al.* Structural basis of kainate subtype glutamate receptor
978 desensitization. *Nature* **537**, 567-571 (2016). https://doi.org:10.1038/nature19352

979 29 Khanra, N., Brown, P. M., Perozzo, A. M., Bowie, D. & Meyerson, J. R. Architecture and
980 structural dynamics of the heteromeric GluK2/K5 kainate receptor. *Elife* **10** (2021).
981 https://doi.org:10.7554/eLife.66097

982 30 He, L. *et al.* Kainate receptor modulation by NETO2. *Nature* (2021).
983 https://doi.org:10.1038/s41586-021-03936-y

984 31 Kumari, J., Vinnakota, R. & Kumar, J. Structural and Functional Insights into GluK3-
985 kainate Receptor Desensitization and Recovery. *Sci Rep* **9**, 10254 (2019).
986 https://doi.org:10.1038/s41598-019-46770-z

987 32 Gangwar, S. P., Yen, L. Y., Yelshanskaya, M. V. & Sobolevsky, A. I. Positive and negative
988 allosteric modulation of GluK2 kainate receptors by BPAM344 and antiepileptic
989 perampanel. *Cell Rep* **42**, 112124 (2023). https://doi.org:10.1016/j.celrep.2023.112124

990 33 Kumari, J. *et al.* Structural dynamics of the GluK3-kainate receptor neurotransmitter
991 binding domains revealed by cryo-EM. *Int J Biol Macromol* **149**, 1051-1058 (2020).
992 https://doi.org:10.1016/j.ijbiomac.2020.01.282

993 34 Gangwar, S. P. *et al.* Trapping of spermine, Kukoamine A, and polyamine toxin blockers
994 in GluK2 kainate receptor channels. *Nat Commun* **15**, 10257 (2024).
995 https://doi.org:10.1038/s41467-024-54538-x

996 35 Paternain, A. V., Rodríguez-Moreno, A., Villarroel, A. & Lerma, J. Activation and
997 desensitization properties of native and recombinant kainate receptors.
998 *Neuropharmacology* **37**, 1249-1259 (1998). https://doi.org:10.1016/s0028-
999 3908(98)00098-7

1000 36 Weston, M. C., Schuck, P., Ghosal, A., Rosenmund, C. & Mayer, M. L. Conformational
1001 restriction blocks glutamate receptor desensitization. *Nat Struct Mol Biol* **13**, 1120-1127
1002 (2006). https://doi.org:10.1038/nsmb1178

1003 37 Jones, M. V. & Westbrook, G. L. The impact of receptor desensitization on fast synaptic
1004 transmission. *Trends Neurosci* **19**, 96-101 (1996). https://doi.org:10.1016/s0166-
1005 2236(96)80037-3

1006 38 Meyerson, J. R. *et al.* Structural mechanism of glutamate receptor activation and
1007 desensitization. *Nature* **514**, 328-334 (2014). https://doi.org:10.1038/nature13603

1008 39 Dhingra, S., Chopade, P. M., Vinnakota, R. & Kumar, J. Functional implications of the
1009 exon 9 splice insert in GluK1 kainate receptors. *Elife* **12** (2024).
1010 https://doi.org:10.7554/eLife.89755

1011 40 Schauder, D. M. *et al.* Glutamate receptor desensitization is mediated by changes in
1012 quaternary structure of the ligand binding domain. *Proc Natl Acad Sci U S A* **110**, 5921-
1013 5926 (2013). https://doi.org:10.1073/pnas.1217549110

1014 41 Twomey, E. C., Yelshanskaya, M. V., Grassucci, R. A., Frank, J. & Sobolevsky, A. I.
1015 Channel opening and gating mechanism in AMPA-subtype glutamate receptors. *Nature*
1016 **549**, 60-65 (2017). https://doi.org:10.1038/nature23479

1017 42 Yelshanskaya, M. V., Patel, D. S., Kottke, C. M., Kurnikova, M. G. & Sobolevsky, A. I.
1018 Opening of glutamate receptor channel to subconductance levels. *Nature* **605**, 172-178
1019 (2022). https://doi.org:10.1038/s41586-022-04637-w

1020 43 Chen, S. *et al.* Activation and Desensitization Mechanism of AMPA Receptor-TARP
1021 Complex by Cryo-EM. *Cell* **170**, 1234-1246.e1214 (2017).
1022 https://doi.org:10.1016/j.cell.2017.07.045

1023 44 Waterhouse, A. *et al.* SWISS-MODEL: homology modelling of protein structures and
1024 complexes. *Nucleic Acids Res* **46**, W296-w303 (2018). https://doi.org:10.1093/nar/gky427

1025 45 Bienert, S. *et al.* The SWISS-MODEL Repository-new features and functionality. *Nucleic*
1026 *Acids Res* **45**, D313-d319 (2017). https://doi.org:10.1093/nar/gkw1132

46 Guex, N., Peitsch, M. C. & Schwede, T. Automated comparative protein structure modeling with SWISS-MODEL and Swiss-PdbViewer: a historical perspective. *Electrophoresis* **30 Suppl 1**, S162-173 (2009). https://doi.org:10.1002/elps.200900140

47 Studer, G. *et al.* QMEANDisCo-distance constraints applied on model quality estimation. *Bioinformatics* **36**, 1765-1771 (2020). https://doi.org:10.1093/bioinformatics/btz828

48 Bertoni, M., Kiefer, F., Biasini, M., Bordoli, L. & Schwede, T. Modeling protein quaternary structure of homo- and hetero-oligomers beyond binary interactions by homology. *Sci Rep* **7**, 10480 (2017). https://doi.org:10.1038/s41598-017-09654-8

49 Esmenjaud, J. B. *et al.* An inter-dimer allosteric switch controls NMDA receptor activity. *Embo j* **38** (2019). https://doi.org:10.15252/embj.201899894

50 Salazar, H., Eibl, C., Chebli, M. & Plested, A. Mechanism of partial agonism in AMPA-type glutamate receptors. *Nat Commun* **8**, 14327 (2017). https://doi.org:10.1038/ncomms14327

51 Baranovic, J. & Plested, A. J. Auxiliary subunits keep AMPA receptors compact during activation and desensitization. *Elife* **7** (2018). https://doi.org:10.7554/eLife.40548

52 Plested, A. J. & Mayer, M. L. AMPA receptor ligand binding domain mobility revealed by functional cross linking. *J Neurosci* **29**, 11912-11923 (2009). https://doi.org:10.1523/jneurosci.2971-09.2009

53 Daniels, B. A., Andrews, E. D., Aurousseau, M. R., Accardi, M. V. & Bowie, D. Crosslinking the ligand-binding domain dimer interface locks kainate receptors out of the main open state. *J Physiol* **591**, 3873-3885 (2013). https://doi.org:10.1113/jphysiol.2013.253666

54 Careaga, C. L. & Falke, J. J. Thermal motions of surface alpha-helices in the D-galactose chemosensory receptor. Detection by disulfide trapping. *J Mol Biol* **226**, 1219-1235 (1992). https://doi.org:10.1016/0022-2836(92)91063-u

55 Larsen, A. P. *et al.* Identification and Structure-Function Study of Positive Allosteric Modulators of Kainate Receptors. *Mol Pharmacol* **91**, 576-585 (2017). https://doi.org:10.1124/mol.116.107599

56 Bay, Y. *et al.* The positive allosteric modulator BPAM344 and L-glutamate introduce an active-like structure of the ligand-binding domain of GluK2. *FEBS Lett* **598**, 743-757 (2024). https://doi.org:10.1002/1873-3468.14824

57 Twomey, E. C. & Sobolevsky, A. I. Structural Mechanisms of Gating in Ionotropic Glutamate Receptors. *Biochemistry* **57**, 267-276 (2018). https://doi.org:10.1021/acs.biochem.7b00891

58 Zhou, C. & Tajima, N. Structural insights into NMDA receptor pharmacology. *Biochem Soc Trans* **51**, 1713-1731 (2023). https://doi.org:10.1042/bst20230122

59 Klein, R. M. & Howe, J. R. Effects of the lurcher mutation on GluR1 desensitization and activation kinetics. *J Neurosci* **24**, 4941-4951 (2004). https://doi.org:10.1523/jneurosci.0660-04.2004

1065 60 Wilding, T. J. & Huettner, J. E. Cadmium opens GluK2 kainate receptors with cysteine
1066 substitutions at the M3 helix bundle crossing. *J Gen Physiol* **151**, 435-451 (2019).
1067 https://doi.org:10.1085/jgp.201812234

1068 61 Fleck, M. W., Cornell, E. & Mah, S. J. Amino-acid residues involved in glutamate receptor
1069 6 kainate receptor gating and desensitization. *J Neurosci* **23**, 1219-1227 (2003).
1070 https://doi.org:10.1523/jneurosci.23-04-01219.2003

1071 62 Twomey, E. C., Yelshanskaya, M. V., Grassucci, R. A., Frank, J. & Sobolevsky, A. I.
1072 Structural Bases of Desensitization in AMPA Receptor-Auxiliary Subunit Complexes.
1073 *Neuron* **94**, 569-580.e565 (2017). https://doi.org:10.1016/j.neuron.2017.04.025

1074 63 Klykov, O., Gangwar, S. P., Yelshanskaya, M. V., Yen, L. & Sobolevsky, A. I. Structure
1075 and desensitization of AMPA receptor complexes with type II TARP γ5 and GSG1L. *Mol*
1076 *Cell* **81**, 4771-4783.e4777 (2021). https://doi.org:10.1016/j.molcel.2021.09.030

1077 64 Herguedas, B. *et al.* Mechanisms underlying TARP modulation of the GluA1/2-γ8 AMPA
1078 receptor. *Nat Commun* **13**, 734 (2022). https://doi.org:10.1038/s41467-022-28404-7

1079 65 Gangwar, S. P. *et al.* Modulation of GluA2-γ5 synaptic complex desensitization, polyamine
1080 block and antiepileptic perampanel inhibition by auxiliary subunit cornichon-2. *Nat Struct*
1081 *Mol Biol* **30**, 1481-1494 (2023). https://doi.org:10.1038/s41594-023-01080-x

1082 66 Zhang, D. *et al.* Structural mobility tunes signalling of the GluA1 AMPA glutamate receptor.
1083 *Nature* **621**, 877-882 (2023). https://doi.org:10.1038/s41586-023-06528-0

1084 67 Reiner, A. & Isacoff, E. Y. Tethered ligands reveal glutamate receptor desensitization
1085 depends on subunit occupancy. *Nat Chem Biol* **10**, 273-280 (2014).
1086 https://doi.org:10.1038/nchembio.1458

1087 68 Fisher, M. T. & Fisher, J. L. Contributions of different kainate receptor subunits to the
1088 properties of recombinant homomeric and heteromeric receptors. *Neuroscience* **278**, 70-
1089 80 (2014). https://doi.org:10.1016/j.neuroscience.2014.08.009

1090 69 Salazar, H., Mischke, S. & Plested, A. J. R. Measurements of the Timescale and
1091 Conformational Space of AMPA Receptor Desensitization. *Biophys J* **119**, 206-218 (2020).
1092 https://doi.org:10.1016/j.bpj.2020.05.029

1093 70 Zhang, W. *et al.* A transmembrane accessory subunit that modulates kainate-type
1094 glutamate receptors. *Neuron* **61**, 385-396 (2009).
1095 https://doi.org:10.1016/j.neuron.2008.12.014

1096 71 Swanson, G. T., Feldmeyer, D., Kaneda, M. & Cull-Candy, S. G. Effect of RNA editing and
1097 subunit co-assembly single-channel properties of recombinant kainate receptors. *J*
1098 *Physiol* **492 (Pt 1)**, 129-142 (1996). https://doi.org:10.1113/jphysiol.1996.sp021295

1099 72 Aittoniemi, J., Jensen, M., Pan, A. C. & Shaw, D. E. Desensitization dynamics of the AMPA
1100 receptor. *Structure* **31**, 724-734.e723 (2023). https://doi.org:10.1016/j.str.2023.03.013

1101 73 Carbone, A. L. & Plested, A. J. Coupled control of desensitization and gating by the ligand
1102 binding domain of glutamate receptors. *Neuron* **74**, 845-857 (2012).
1103 https://doi.org:10.1016/j.neuron.2012.04.020

1104 74 Plested, A. J. & Mayer, M. L. Structure and mechanism of kainate receptor modulation by
1105 anions. *Neuron* **53**, 829-841 (2007). https://doi.org:10.1016/j.neuron.2007.02.025

1106 75 Mondal, A. K., Carrillo, E., Jayaraman, V. & Twomey, E. C. Temperature Sensitive
1107 Glutamate Gating of AMPA-subtype iGluRs. *bioRxiv* (2024).
1108 https://doi.org:10.1101/2024.09.05.611422

1109 76 Dürr, K. L. *et al.* Structure and dynamics of AMPA receptor GluA2 in resting, pre-open,
1110 and desensitized states. *Cell* **158**, 778-792 (2014).
1111 https://doi.org:10.1016/j.cell.2014.07.023

1112 77 Ivica, J. *et al.* Proton-triggered rearrangement of the AMPA receptor N-terminal domains
1113 impacts receptor kinetics and synaptic localization. *Nat Struct Mol Biol* **31**, 1601-1613
1114 (2024). https://doi.org:10.1038/s41594-024-01369-5

1115 78 Larsen, A. H., Perozzo, A. M., Biggin, P. C., Bowie, D. & Kastrup, J. S. Recovery from
1116 desensitization in GluA2 AMPA receptors is affected by a single mutation in the N-terminal
1117 domain interface. *J Biol Chem* **300**, 105717 (2024).
1118 https://doi.org:10.1016/j.jbc.2024.105717

1119 79 Coombs, I. D. *et al.* Homomeric GluA2(R) AMPA receptors can conduct when
1120 desensitized. *Nat Commun* **10**, 4312 (2019). https://doi.org:10.1038/s41467-019-12280-9

1121 80 Revah, F. *et al.* Mutations in the channel domain alter desensitization of a neuronal
1122 nicotinic receptor. *Nature* **353**, 846-849 (1991). https://doi.org:10.1038/353846a0

1123 81 Bowie, D. & Lange, G. D. Functional stoichiometry of glutamate receptor desensitization.
1124 *J Neurosci* **22**, 3392-3403 (2002). https://doi.org:10.1523/jneurosci.22-09-03392.2002

1125 82 Dawe, G. B. *et al.* Defining the structural relationship between kainate-receptor
1126 deactivation and desensitization. *Nat Struct Mol Biol* **20**, 1054-1061 (2013).
1127 https://doi.org:10.1038/nsmb.2654

1128

1129

1130

1131

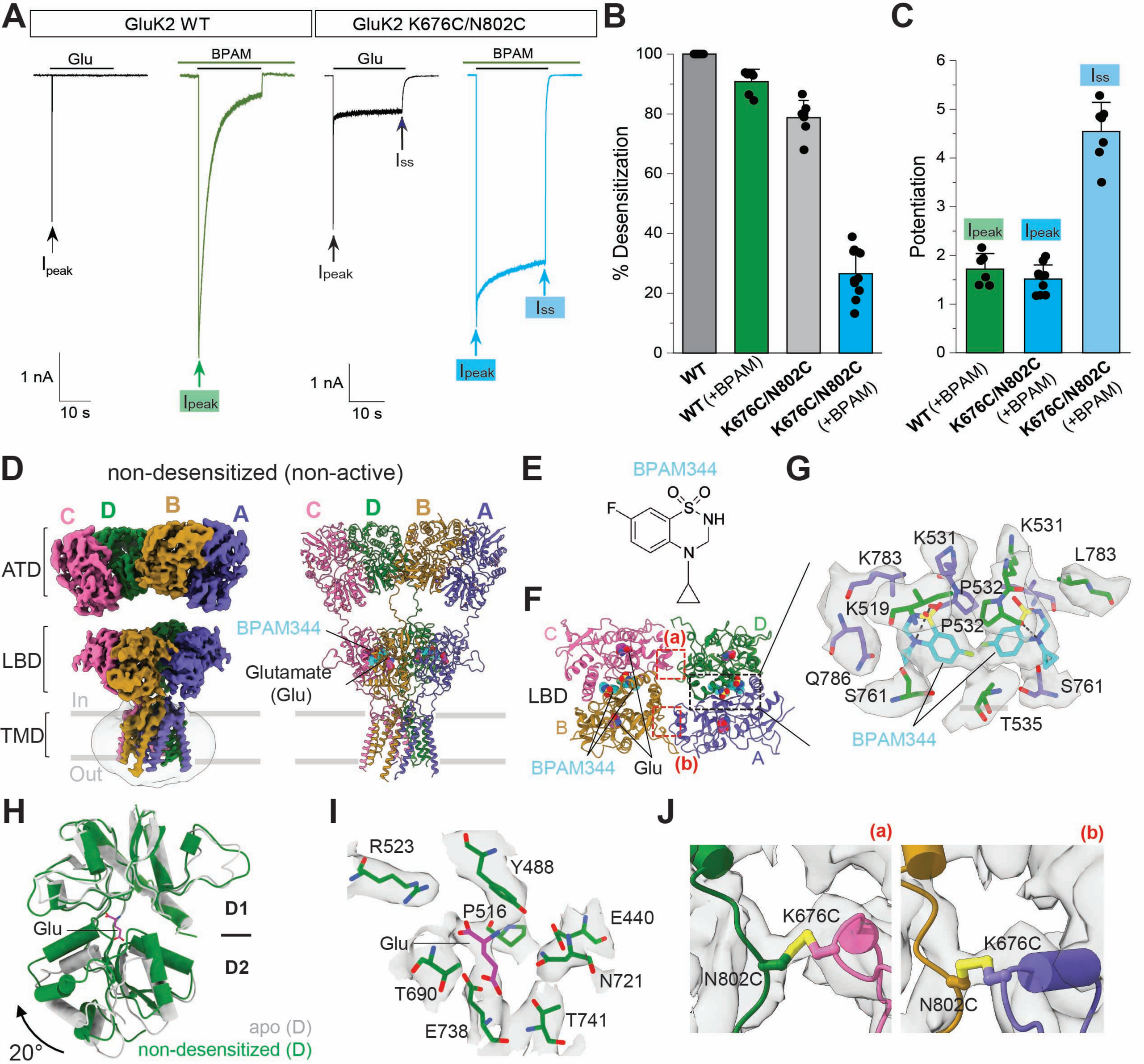
A
GluK2 WT
GluK2 K676C/N802C
Glu
BPAM
Ipeak
Iss
1 nA
10 s
B
% Desensitization
WT
WT (+BPAM)
K676C/N802C
K676C/N802C (+BPAM)
C
Potentiation
D
non-desensitized (non-active)
ATD
LBD
TMD
In
Out
BPAM344
Glutamate (Glu)
E
F
(a)
(b)
G
K783
K531
L783
K519
P532
Q786
S761
T535
H
D1
D2
apo (D)
non-desensitized (D)
20°
I
R523
Y488
P516
E440
N721
T690
T741
E738
J
K676C
N802C

Figure 1

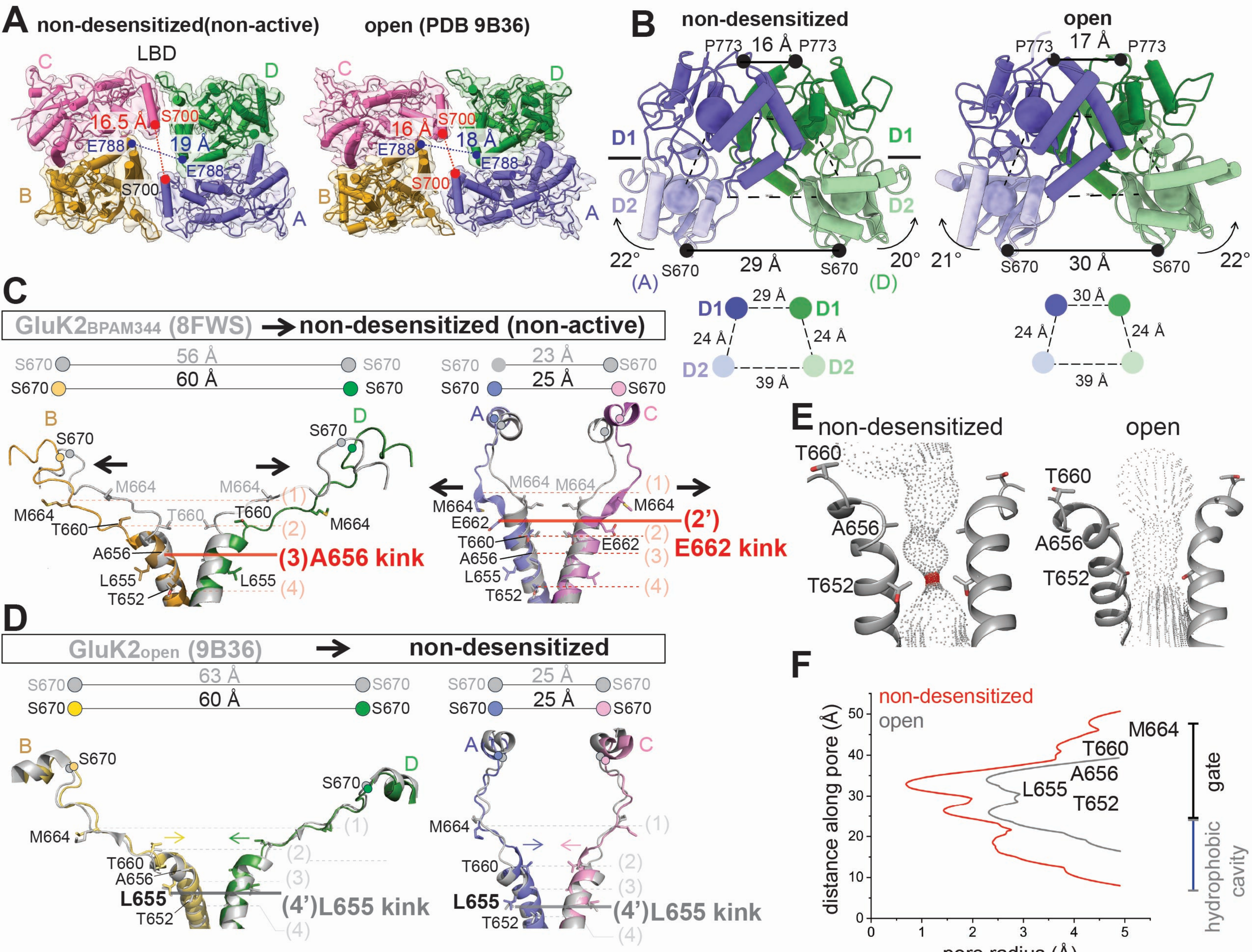
A
non-desensitized(non-active)
open (PDB 9B36)
LBD
C
D
B
A
16.5 Å
S700
E788
19 Å
16 Å
18 Å
B
non-desensitized
open
P773
16 Å
17 Å
D1
D2
22°
20°
21°
S670
29 Å
30 Å
(A)
(D)
24 Å
39 Å
C
GluK2BPAM344 (8FWS) → non-desensitized (non-active)
56 Å
60 Å
23 Å
25 Å
M664
T660
A656
L655
T652
E662
(1)
(2)
(3)A656 kink
(2')
E662 kink
(3)
(4)
D
GluK2open (9B36) → non-desensitized
63 Å
60 Å
25 Å
25 Å
(4')L655 kink
E
non-desensitized
open
T660
A656
T652
F
non-desensitized
open
distance along pore (Å)
pore radius (Å)
M664
T660
A656
L655
T652
gate
hydrophobic cavity

Figure 2

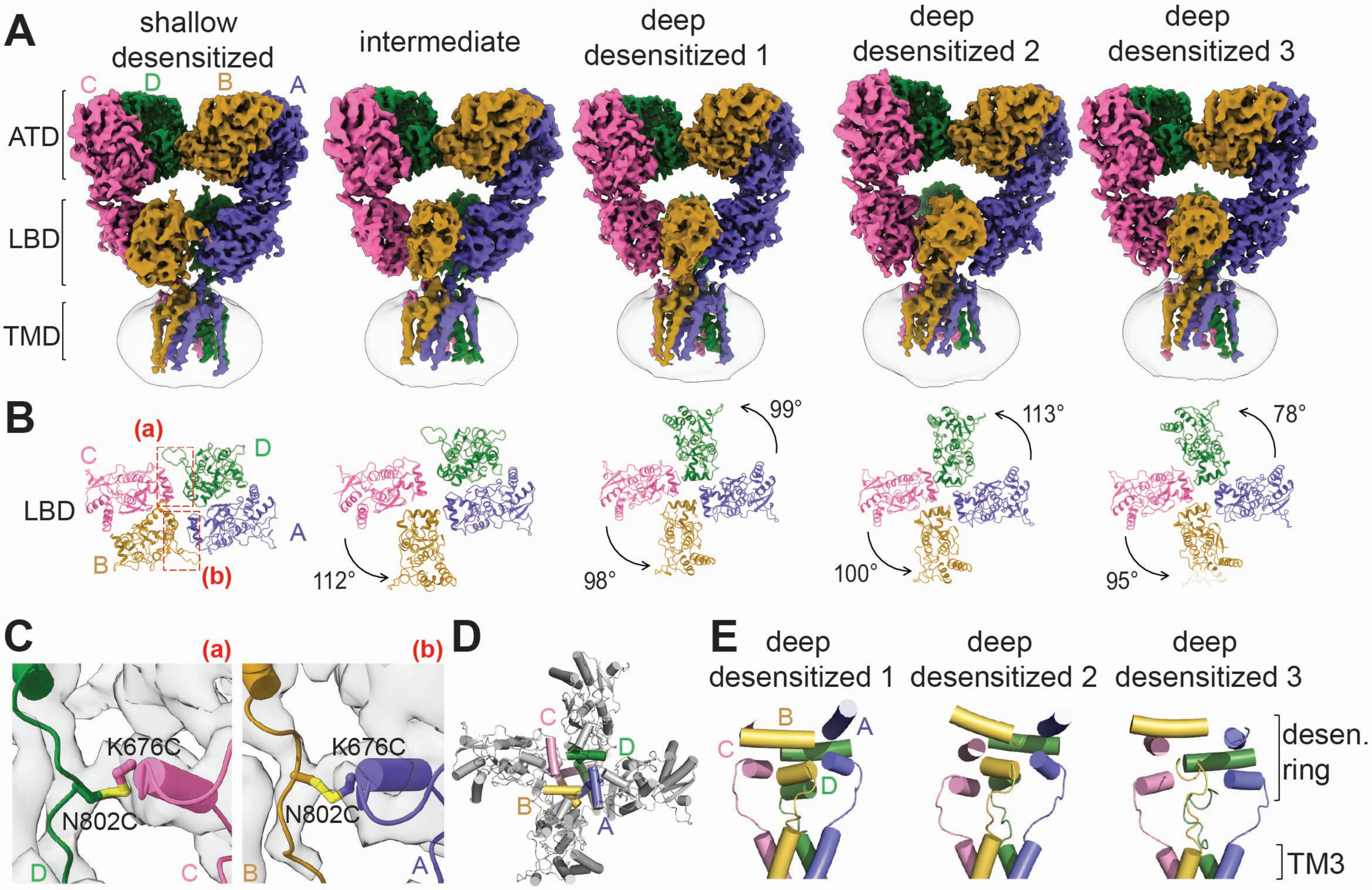
A
shallow desensitized
intermediate
deep desensitized 1
deep desensitized 2
deep desensitized 3
C
D
B
A
ATD
LBD
TMD
B
(a)
(b)
LBD
112°
98°
99°
100°
113°
95°
78°
C
K676C
N802C
D
E
desen. ring
TM3

Figure 3

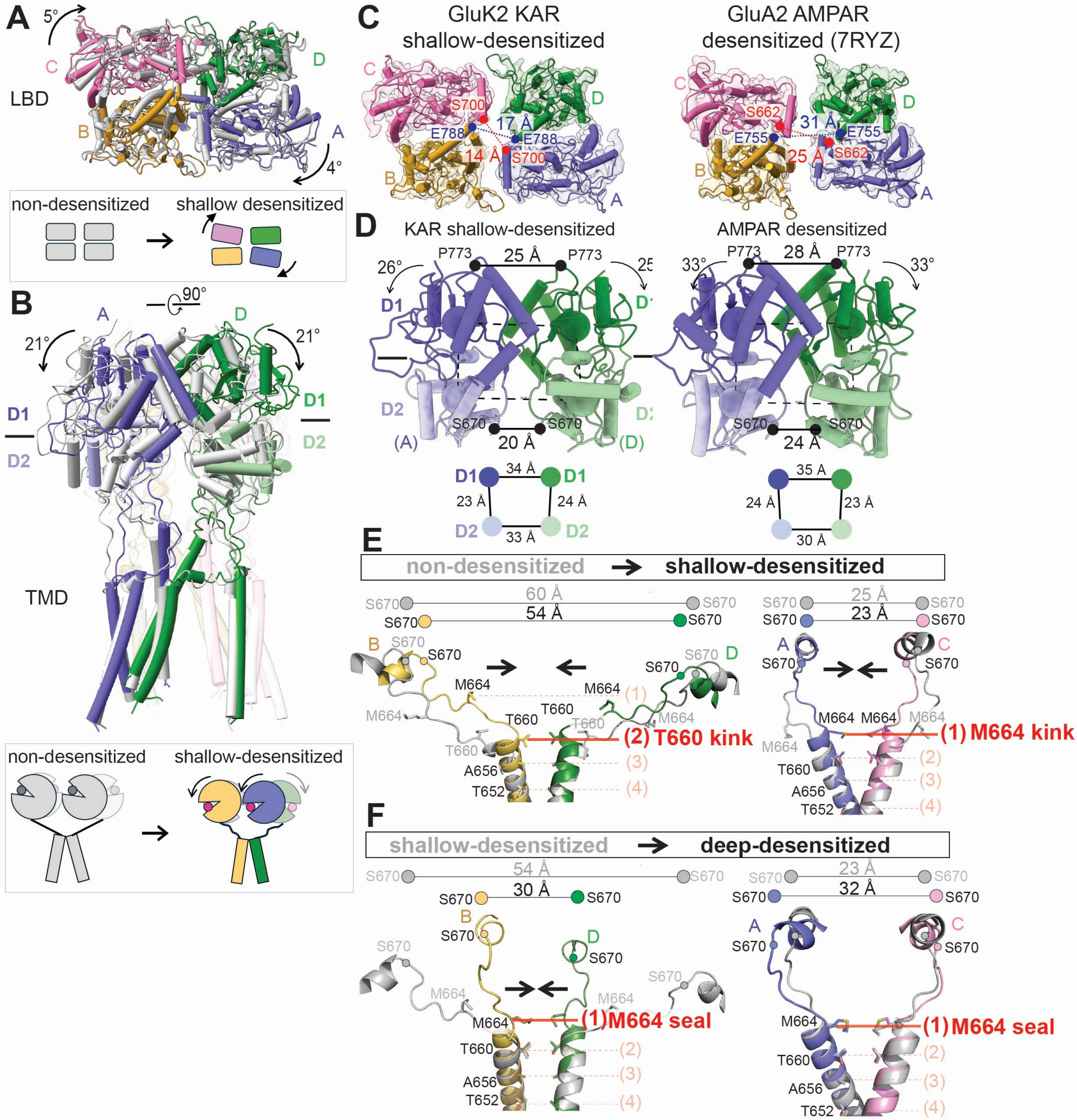
A
5°
C
D
LBD
B
A
4°
non-desensitized
shallow desensitized
B
90°
A
D
21°
21°
D1
D1
D2
D2
TMD
non-desensitized
shallow-desensitized
C
GluK2 KAR
shallow-desensitized
GluA2 AMPAR
desensitized (7RYZ)
S700
17 Å
E788
E788
14 Å
S700
S662
31 Å
E755
E755
25 Å
S662
D
KAR shallow-desensitized
AMPAR desensitized
P773
25 Å
P773
26°
P773
28 Å
P773
33°
33°
D1
D2
S670
S670
20 Å
(A)
(D)
S670
S670
24 Å
D1
34 Å
D1
23 Å
24 Å
D2
33 Å
D2
35 A
24 Å
23 Å
30 Å
E
non-desensitized
shallow-desensitized
60 Å
54 Å
S670
S670
B
M664
T660
T660
T660
M664
M664
(1)
(2) T660 kink
(3)
(4)
A656
T652
25 Å
23 Å
A
C
M664
M664
M664
(1) M664 kink
(2)
(3)
(4)
F
shallow-desensitized
deep-desensitized
54 Å
30 Å
23 Å
32 Å
S670
B
D
M664
M664
(1) M664 seal
T660
(2)
(3)
A656
T652
(4)
A
C
M664
(1) M664 seal
T660
(2)
(3)
A656
T652
(4)

Figure 4

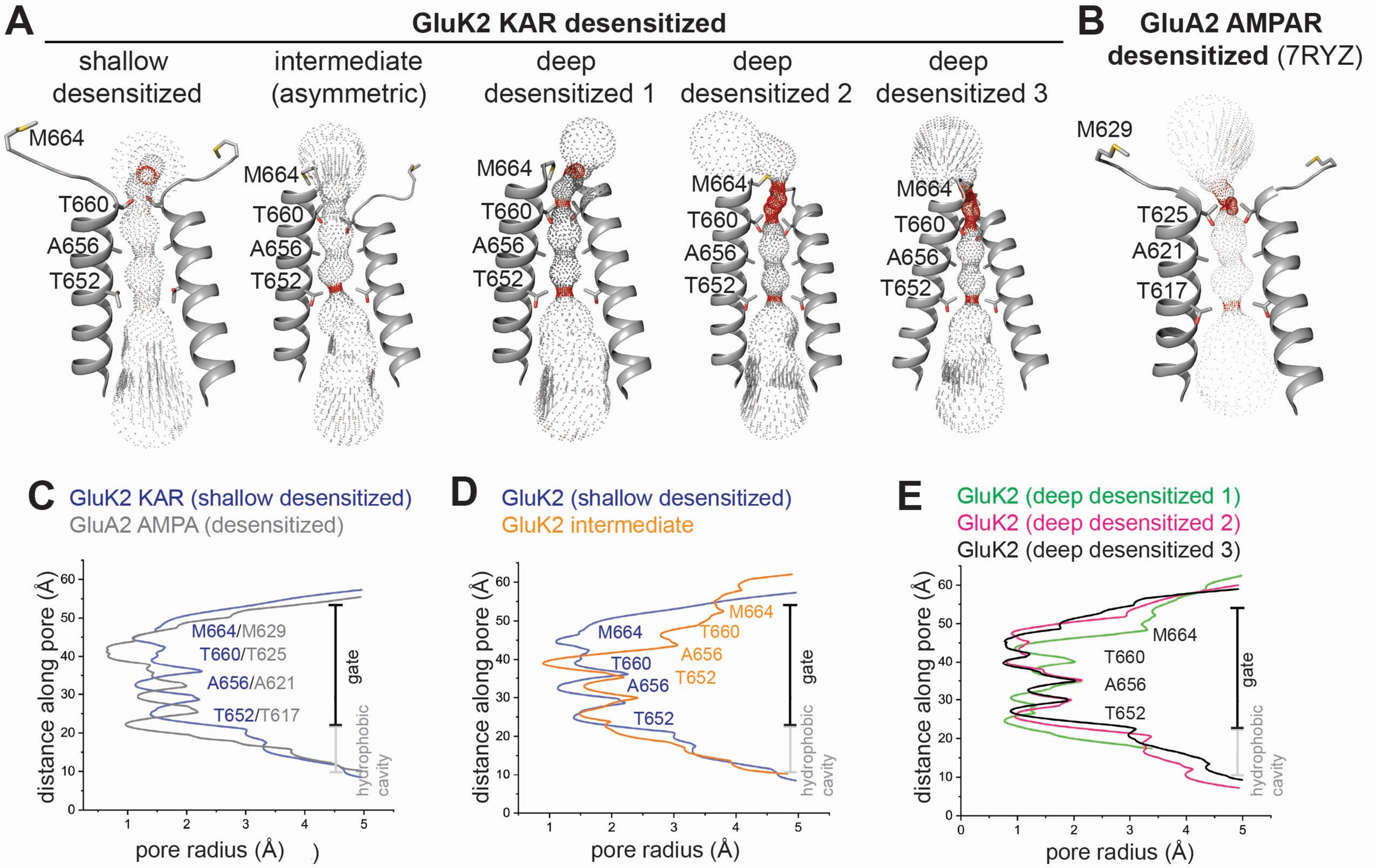
A
GluK2 KAR desensitized
shallow desensitized
intermediate (asymmetric)
deep desensitized 1
deep desensitized 2
deep desensitized 3
M664
T660
A656
T652
B
GluA2 AMPAR desensitized (7RYZ)
M629
T625
A621
T617
C
GluK2 KAR (shallow desensitized)
GluA2 AMPA (desensitized)
M664/M629
T660/T625
A656/A621
T652/T617
gate
hydrophobic cavity
distance along pore (Å)
pore radius (Å)
D
GluK2 (shallow desensitized)
GluK2 intermediate
E
GluK2 (deep desensitized 1)
GluK2 (deep desensitized 2)
GluK2 (deep desensitized 3)

Figure 5

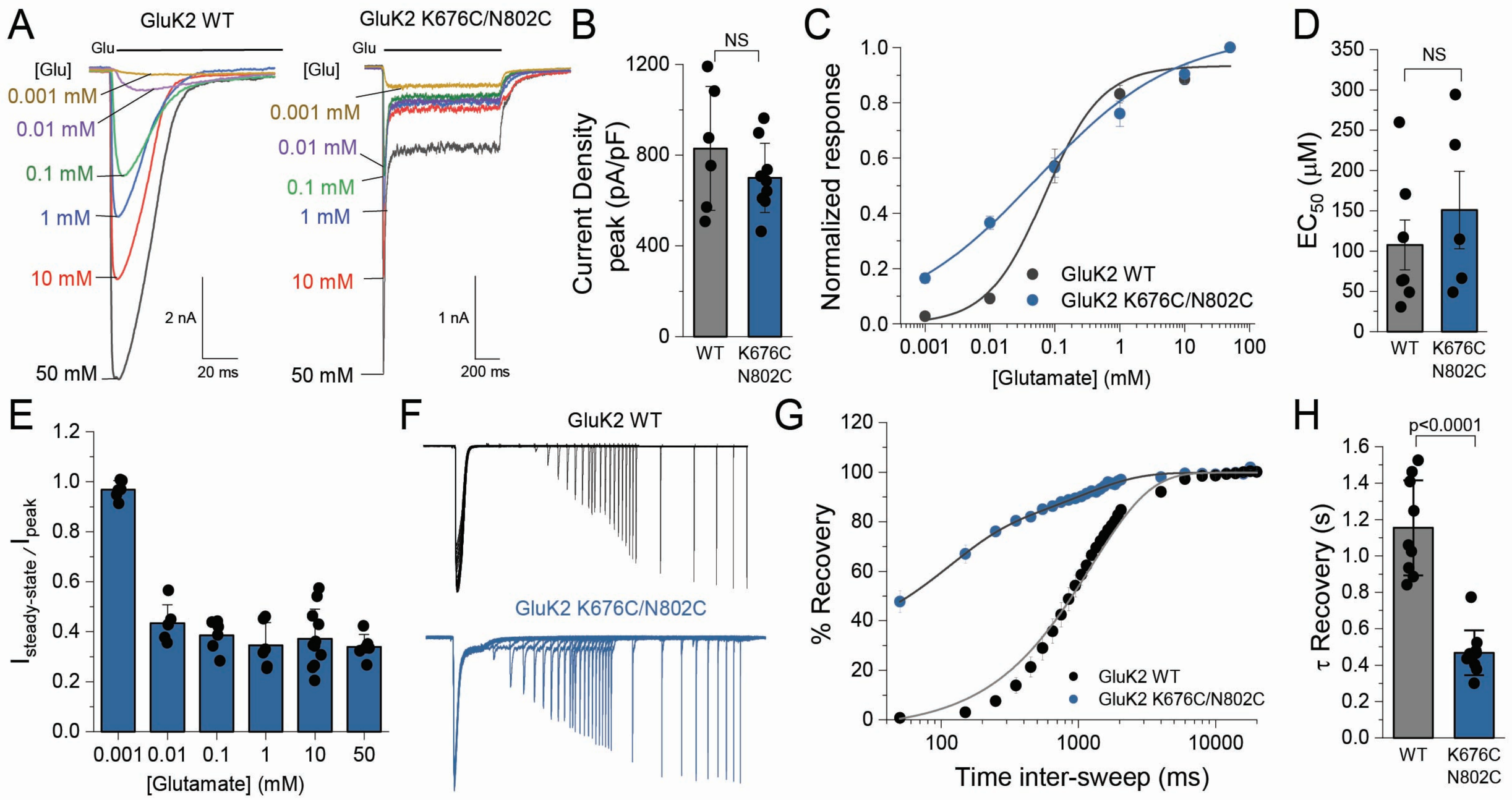
A
GluK2 WT
GluK2 K676C/N802C
Glu
[Glu]
0.001 mM
0.01 mM
0.1 mM
1 mM
10 mM
50 mM
2 nA
20 ms
1 nA
200 ms
B
NS
Current Density peak (pA/pF)
WT
K676C N802C
C
Normalized response
[Glutamate] (mM)
GluK2 WT
GluK2 K676C/N802C
D
NS
EC50 (µM)
WT
K676C N802C
E
Isteady-state / Ipeak
[Glutamate] (mM)
F
GluK2 WT
GluK2 K676C/N802C
G
% Recovery
Time inter-sweep (ms)
GluK2 WT
GluK2 K676C/N802C
H
p<0.0001
τ Recovery (s)
WT
K676C N802C

Figure 6

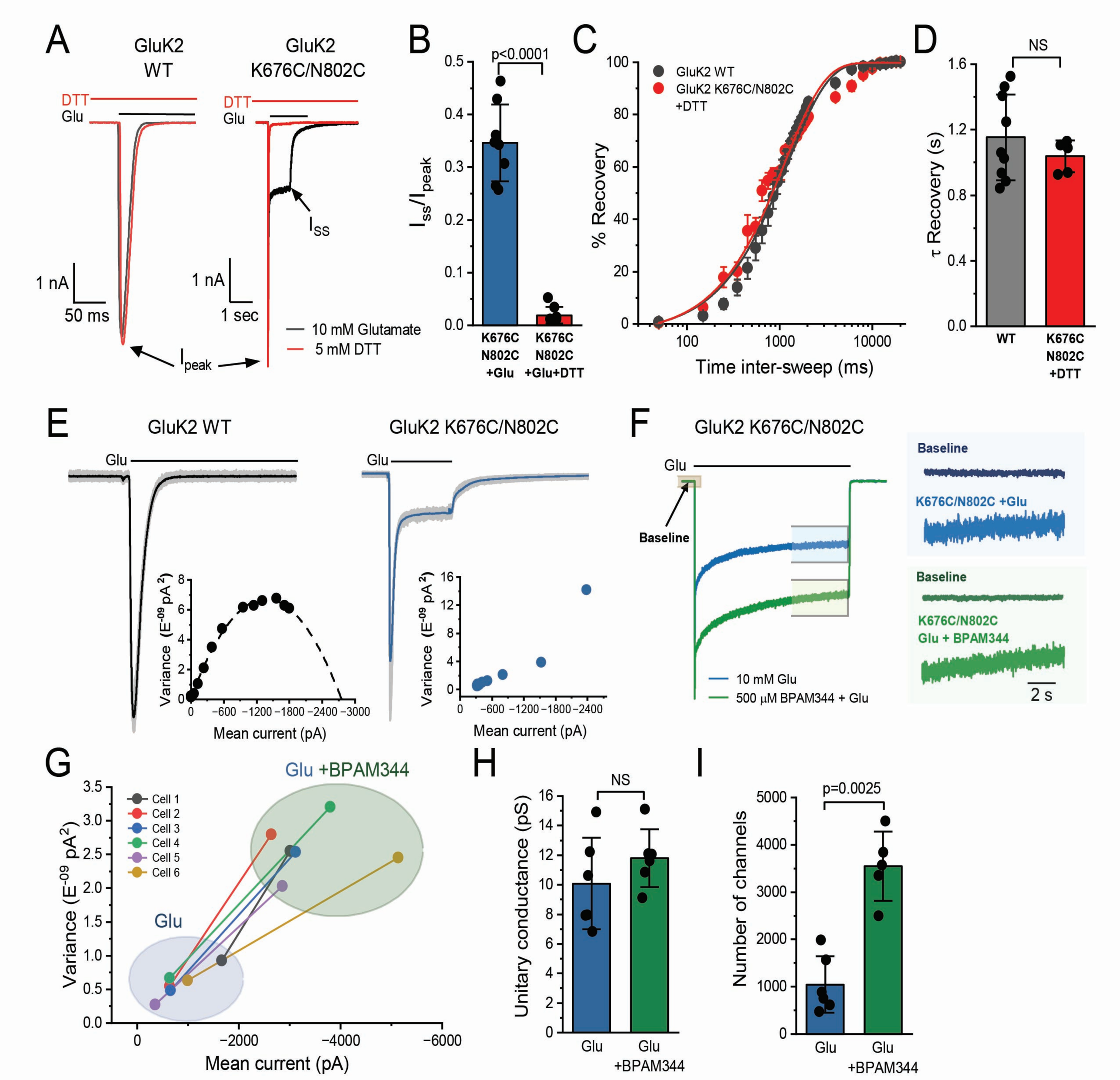
A
GluK2 WT
GluK2 K676C/N802C
DTT
Glu
1 nA
50 ms
1 sec
I_{peak}
I_{SS}
10 mM Glutamate
5 mM DTT
B
p<0.0001
I_{ss}/I_{peak}
K676C N802C +Glu
K676C N802C +Glu+DTT
C
GluK2 WT
GluK2 K676C/N802C +DTT
% Recovery
Time inter-sweep (ms)
D
NS
τ Recovery (s)
WT
K676C N802C +DTT
E
GluK2 WT
GluK2 K676C/N802C
Variance (E^{-09} pA^2)
Mean current (pA)
F
GluK2 K676C/N802C
Baseline
10 mM Glu
500 μM BPAM344 + Glu
K676C/N802C +Glu
K676C/N802C Glu + BPAM344
2 s
G
Glu +BPAM344
Glu
Cell 1
Cell 2
Cell 3
Cell 4
Cell 5
Cell 6
Variance (E^{-09} pA^2)
Mean current (pA)
H
NS
Unitary conductance (pS)
Glu
Glu +BPAM344
I
p=0.0025
Number of channels
Glu
Glu +BPAM344

Figure 7

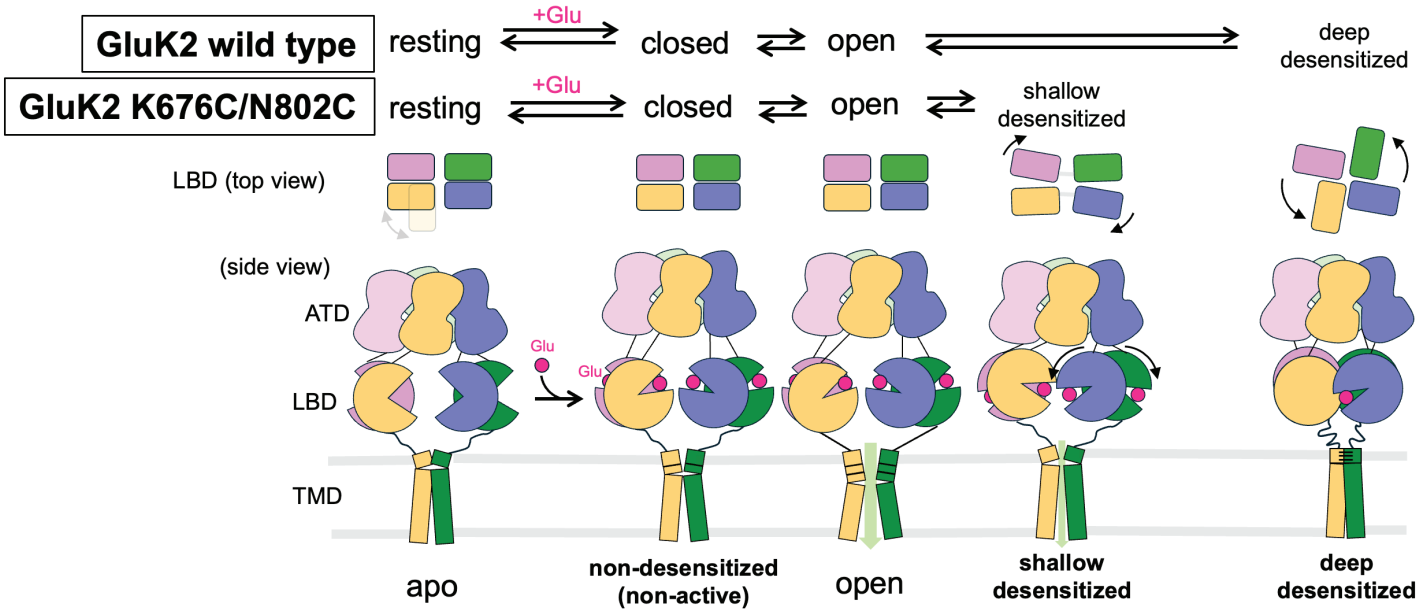
GluK2 wild type
resting
+Glu
closed
open
deep desensitized
GluK2 K676C/N802C
resting
+Glu
closed
open
shallow desensitized
LBD (top view)
(side view)
ATD
LBD
TMD
Glu
Glu
apo
non-desensitized (non-active)
open
shallow desensitized
deep desensitized

Figure 8